J. Fluid Mech. (1981), *vol.* 105, *pp.* 87–117
Printed in Great Britain

On the structure of turbulent flow over a progressive water wave: theory and experiment in a transformed, wave-following co-ordinate system

By CHIN-TSAU HSU,† EN YUN HSU AND ROBERT L. STREET

Department of Civil Engineering,
Stanford University, California 94305

(Received 22 February 1978 and in revised form 21 April 1980)

An investigation of the turbulent flow structure over a progressive water wave, as well as the structure of the wave-induced flow field in a transformed wave-following frame, is reported. Experimental results are given for a free-stream velocity of 2·4 m s^{-1} over a 1 Hz mechanically generated deep-water wave. The velocity components were measured with a cross hot-film probe oscillating in a transformed wave-following frame. The amplitude and phase of the wave-induced velocity components are deduced by correlation to the generated water wave. The mean flow tends to follow the wave form so that the water wave should not be regarded as surface roughness. The mean velocity profile is basically log-linear and is similar to that over a smooth plate, because ripples riding on the waves do not produce sufficient roughness to interfere with the wind field. The wave-induced motion in the free stream is irrotational; but, in the boundary layer, it has strong shear behaviour related to the wave-associated Reynolds stress. The shear stress production as well as the energy production from the mean flow is concentrated near the interface. A phase jump of 180° in the wave-induced turbulent Reynolds stresses in the middle of the boundary layer was observed. The relationships between the induced turbulent Reynolds stresses and the induced velocities are of an eddy-viscosity type.

1. Introduction

The theory of water-wave generation by the wind was advanced significantly by Phillips (1957) and Miles (1957). Phillips' theory can be regarded as a discussion of an ensemble of surface disturbances excited by turbulent pressure fluctuations. Its mechanism is based on resonance, the resulting wave growth rate is linear, and the theory appears most applicable to the very early growth or the initiation period for the water waves. Miles' theory describes the coupling between surface waves and the mean air flow. The growth mechanism depends mainly on the feedback from the wave-induced air-flow perturbations to the surface waves. His mechanism bears a strong resemblance to classical work on hydrodynamic stability, and the resulting wave growth rate is exponential. Hence, Miles' mechanism is more effective than Phillips' mechanism in transferring energy from wind to waves. It was anticipated that Miles'

† Now at Fluid Mechanics Department, TRW/DSSG, One Space Park, Redondo Beach, California.

mechanism would provide an explanation for the major portion of energy transfer; unfortunately, the measurements of Snyder & Cox (1966), Barnett & Wilkerson (1967) and Bole & Hsu (1969) showed measured growth rates which were up to an order of magnitude greater than those predicted from Miles' theory.

Although Miles acknowledged the possible significance of the induced turbulent Reynolds stresses and the ambiguity of the interface boundary conditions caused by using a fixed co-ordinate system in his 1957 paper, he based his calculations primarily on inviscid quasi-laminar assumptions and neglected the viscous and the turbulence effects. The difficulty of the interface boundary conditions was overcome by Miles (1959) and by Benjamin (1959) through the use of transformed co-ordinate systems in which the boundary conditions could be evaluated directly at the interface.

The significance of the induced turbulent Reynolds stresses was implicit in the failure of the quasi-laminar model to predict the major portion of wave growth, and was also demonstrated by Longuet-Higgins (1969) following the concepts given by Stewart (1967). Longuet-Higgins (1969) showed that an oscillating shear stress at the interface could be as important as the wave-induced pressure in transferring the energy to the waves. Kendall (1970) demonstrated experimentally the strong modulation of turbulent structure caused by progressive surface waves on a flexible, but solid wall and the significance of direct energy transfer to the waves as they were acted upon by the induced turbulent Reynolds stresses.

When the induced turbulent Reynolds stresses are retained in the linearized perturbation equations, the closure problem impedes any further theoretical predictions. Closure relations were obtained by several authors using the existing closure theories in turbulence. Among them are Miles (1967), Long (1971), Davis (1970, 1972), Townsend (1972), Saeger & Reynolds (1971), Norris & Reynolds (1975), Gent & Taylor (1976) and Gent (1977). The predictions of their models were compared with the measurements of Stewart (1970), Kendall (1970), Dobson (1971), Elliott (1972), Hasselmann *et al.* (1973), Snyder (1974) and others. However, the comparisons led to no conclusive results in regard to wave-generation theory. Accordingly, the problem of how the wave is generated by wind requires further investigation. The main reasons for this are two-fold.

First, there exists a wide inconsistency among the measured results. In comparison of wave growth rates, Snyder's (1974) data agreed with that of Miles' prediction, Elliott's (1972) were twice that of Miles', and Dobson's (1971) were one order in magnitude greater than Miles' predictions. Because these three sets of results were all resolved from pressure-field measurement above the ocean waves, Snyder (1974, p. 526) suggested that one possibility for this discrepancy was 'At least one, and perhaps all three, of the measurements are wrong'. Snyder also found no explanation that could account for the difference between his data and those of Dobson. Because Dobson's wave growth rates were consistent with those obtained from the direct observations of the wave field by Snyder & Cox (1966)† and by Barnett & Wilkerson (1967), the degree of importance of the role of the wave-induced pressure in wave generation is still unknown. Dobson & Elliott (1978) report that recent field pressure measurements indicate that Dobson's (1971) value of the growth rate factor β is too

† This agreement is now considered surprising because Dobson measured energy input from the wind only, while Snyder & Cox measured energy input from all sources, including nonlinear wave–wave interactions.

high by a factor of 3 and that Elliott's measurements are closest to correct. The confusion is compounded by the work of JONSWAP (Hasselmann *et al.* 1973), where the major wave growth could be explained by a nonlinear theory of wave–wave interaction.

Second, there exists no acceptable data set for the wave-induced turbulent Reynolds stresses as a basis for closure modelling. All the closure models have been based on *ad hoc* or phenomenological assumptions from existing turbulent closure theory. Whether the closure for a turbulent flow in a solid wall channel can be applied equally to an interface flow, where there are progressive water waves, is still questionable. This, together with the incompleteness of our knowledge of turbulence, has substantially limited the applicability of the models. To gain a clear insight to the closure modelling for the perturbation field, a complete and direct measurement of the air flow field including the induced turbulent Reynolds stresses was needed.

By reviewing the methods of approach in the works cited above, one finds that they can be categorized into two types. One is the fixed-frame measurement or analysis and the other is the wave-following frame measurement or analysis. The data of Dobson were collected by a wave-following buoy and the analyses of Miles (1959), Benjamin (1959), Norris & Reynolds (1975) and Gent & Taylor (1976) were performed in transformed co-ordinate systems; hence, they are wave-following frame approaches. The others use the fixed-frame approach. The differences in physical meanings for flow quantities obtained in these two frames are subtle and seem not to have been discussed properly. The wave-following data have even sometimes been used indiscriminately to check the theoretical results derived in the fixed frame and vice versa. Gent & Taylor (1976, p. 124) stated 'Similar features are found if we plot our results in this way (in the sense of fixed frame†) but merely serve to illustrate how difficult it is to interpret measurements made at a fixed height compared with those from wave-following instruments.' We feel that identifying the differences between flow quantities in the two frames is important if one wishes to obtain a clearer picture of the interface flow structure. Thus, we focus on these differences in this study.

In the present investigation, the characteristics of air flow over a 1 Hz mechanically-generated water wave in the Stanford Wind, Water-Wave Research Facility were obtained by hot-film probe measurements of the air flow and interface characteristics were obtained by wave-height gauge measurements of the water surface. The hot-film probe was mounted on a wave-follower device operating in a transformed co-ordinate system which resembles the one used by Norris & Reynolds (1975). In this paper we attempt to give a clear picture of the physical meaning of quantities obtained in the wave-following frame. The advantages of using a transformed frame over a fixed frame are thus revealed. In particular the transformed frame facilitates the interpretation of the laboratory data. These data include mean and wave perturbation flow fields together with the induced turbulent Reynolds stresses.

The structure of our text is as follows. Section 2 contains the appropriate averaging and decomposition techniques, the transformed wave-following co-ordinate system, and the resulting equations of motion. A brief description of the experimental apparatus and data analysis procedure is in § 3. In § 4 the experimental results are presented, while in § 5 the implications of the results are discussed with a focus on the mean flow

† Present authors' interpretation.

structure, comparison of fixed and transformed frame results, and the momentum and energy transfer. Finally, § 6 offers a summary of our conclusions.

2. Theoretical aspects of wave perturbations

2.1. *Averaging and decomposition*

The time average of a flow quantity $g(\mathbf{x}, t)$ is defined conventionally as

$$G(\mathbf{x}) = \bar{g}(\mathbf{x}) = \lim_{T\to\infty} \frac{1}{T} \int_{-\frac{1}{2}T}^{\frac{1}{2}T} g(\mathbf{x}, t)\, dt. \tag{2.1}$$

The notation G is used when g represents a single variable such as u, v and p; $\bar{g}$ is then used for a product quantity such as $\overline{u_i' u_j'}$. When g contains periodic oscillations as are considered in this study, a conditional average of g, called the 'phase average' and denoted by $\langle g \rangle$, is defined by

$$\langle g(\mathbf{x}, t) \rangle = \lim_{N\to\infty} \frac{1}{2N+1} \sum_{n=-N}^{N} g(\mathbf{x}, t + n\tau), \tag{2.2}$$

where τ is the period of the organized oscillation. The organized wave component of g, denoted by $\tilde{g}$, is defined by

$$\tilde{g} = \langle g \rangle - \bar{g}. \tag{2.3}$$

An arbitrary random signal g can then be represented as

$$g(\mathbf{x}, t) = \bar{g}(\mathbf{x}) + \tilde{g}(\mathbf{x}, t) + g'(\mathbf{x}, t) \tag{2.4}$$

where g' is the fluctuation around the phase average; g' is usually regarded as the background turbulence. The properties of the time and the phase averages can be found in Hussain & Reynolds (1970).

In (2.1) and (2.2) the position $\mathbf{x}$ has to be specified during the course of the averaging processes. When the flow is described in an inertial fixed frame, $\mathbf{x} = (x, y, z)$ is a fixed physical position. On the other hand, a co-ordinate system, $\mathbf{x} = (x^*, y^*, z^*)$, may be prescribed in which the actual physical position changes with time during averaging although the co-ordinates (x^*, y^*, z^*) are constant. Accordingly, the values $\bar{g}$, $\langle g \rangle$ and $\tilde{g}$ must depend on which of the co-ordinate systems is used.

2.2. *Transformed wave-following co-ordinate system*

In this study, we consider a turbulent channel flow of air over a small-amplitude progressive surface water wave $\tilde{\eta}$ with an amplitude a and a period τ. Here, by small amplitude, we mean the wave slope ka is small ($\lesssim 0{\cdot}1$). An *infinitesimal wave* is referred to then as the limiting case where the wave amplitude approaches zero with k fixed. The fixed frame (x, y, z) which is the reference for (x^*, y^*, z^*), is chosen such that x is in the direction of the wind and the wave propagation, y is in the vertical direction measured upward from the mean water level, and z is in the lateral (transverse) direction in accordance with a right-handed system.

For $y < a$, a time-averaged quantity $\bar{g}(x, y, z)$ for the air flow does not exist in a useful form because the fixed position (x, y, z) is sometimes in the water and sometimes in the air, depending on the wave motion; hence, the determination of $\tilde{g}(x, y, z)$ from (2.3) is not possible. As a result, the wave perturbation equations which describe the

wave-induced air motion, in the fixed frame, are not valid when $y < a$ unless one can create a useful description for $\bar{g}(x, y, z)$ in this region (see Phillips 1977, p. 118).

One way to resolve the problem is to apply a traditional perturbation scheme; however, this requires the surface water wave to be infinitesimal. The boundary conditions for $\tilde{u}(x, y, t)$ and $\tilde{v}(x, y, t)$ are obtained at $y = 0$ by extrapolation from $y = \tilde{\eta}$. The flow region becomes then $y \geqslant 0$ and $\bar{g}$ can be defined uniquely. It is well known that this procedure leads to ambiguity because its solution does not describe the flow variation with phase near the interface accurately and cannot be tested directly by experiment. Under what conditions the perturbation scheme and the extrapolation are valid is an interesting subject and deserves further discussion.

Another way to resolve the interface problem is to transform the entire problem to a new co-ordinate system such that both the interface and the upper boundary of the flow are fixed in the new co-ordinates. The use of a co-ordinate transformation enables us to describe completely, not only the entire flow region, but also the interface boundary condition. Hence, there is less ambiguity. In addition, closure models constructed in the transformed frame are based on flow properties, such as eddy viscosity, mixing length, etc., determined relative to the instantaneous water surface rather than the mean water level.

Co-ordinate transformations for interface flow problems can be categorized into two types. The first type uses a curvilinear orthogonal co-ordinate system and transforms the co-ordinate system and the flow field variables so that the velocity components are aligned with the axes of the new co-ordinate system, i.e. 'curvilinear orthogonal' velocities are matched to the curvilinear orthogonal co-ordinate system (Miles 1959; Benjamin 1959; Gent & Taylor 1976; Gent 1977). This alignment can simplify the theoretical analysis; however, a great disadvantage arises relative to experiments because it is a very difficult task to move a probe so as to obtain, for example, velocity components aligned with the axes of the new co-ordinate system *and* at a constant value of the spatial co-ordinates (say x^*, y^*, z^*). If one does not meet the second criteria, data are quite impossible to interpret. Thus, the theoretical works using this type of co-ordinate usually remain experimentally untested. The second type of approach transforms only the co-ordinate system, but not the flow, so that the flow system is regarded as the Cartesian velocity field described in a curvilinear co-ordinate system (Norris & Reynolds 1975). In such a system, probes can be carried quite easily at constant (x^*, y^*, z^*) locations.

In the wave-generation problem, the simplest co-ordinate transformation of the second type which meets our needs is one which contains only vertical translation, namely

$$t = t^*, \quad x = x^*, \quad y = y^* + f(y^*)\,\tilde{\eta}, \quad z = z^* \qquad (2.5a, b, c, d)$$

where

$$\tilde{\eta} = a\cos(kx^* - \omega t^*). \qquad (2.6)$$

It follows that an experimental probe need only be oscillated vertically to lie always at (x^*, y^*, z^*) = constant points. The transformation between (x, y, z) and (x^*, y^*, z^*) is one to one if $f(y^*)$ is monotonic, but is not orthogonal. Any function which gives $f(0) = 1$ and decreases monotonically to zero at the upper boundary of the flow will

do. To maintain the spirit of and to relate our transformation to the transformations of the first type noted above, $f(y^*)$ is chosen to be

$$f(y^*) = \frac{\sinh(kH - ky^*)}{\sinh(kH)} \tag{2.7}$$

Here, $y = y^* = H$ corresponds to the roof of the laboratory wind-wave channel. According to the vertical transformation, (2.5c) surfaces $y^* =$ constant are streamlines of an inviscid flow above a progressive wave without wind (as implied by Benjamin 1959); (2.5c) matches Benjamin's transformation when $H \to \infty$. The co-ordinate system (x^*, y^*, z^*, t^*) given by (2.5)–(2.7) is only slightly different from that used by Norris & Reynolds (1975).

2.3. *Governing equations in the transformed co-ordinate system*

An initial examination of an application of a transformation similar to (2.5) was made by Norris & Reynolds (1975). However, their co-ordinate transformation was applied after the averaged equations had been obtained in (x, y, z, t) and after the closure relations for the wave-induced turbulent Reynolds stresses had been imposed. Some important features of the flow are lost in such an approach for the wind-wave case.

In our analysis, the full unaveraged continuity and Navier–Stokes equations are expressed first in the (x^*, y^*, z^*, t^*) system by application of the chain rule for partial derivatives. The resulting equations are averaged at fixed values of (x^*, y^*, z^*) according to (2.1)–(2.3). Then, the mean flow equations and the wave perturbation equations in (x^*, y^*, z^*, t^*) can be found through the basic procedure used in a fixed-frame analysis. We assume that the flow is fully developed† and that the wave-induced flow is two-dimensional $(\tilde{u}, \tilde{v})$ and a function of x^*, y^* and t^* only. The small-amplitude wave assumption ensures that $\tilde{u}_i = O(k\tilde{\eta})$ so that linearization of the wave perturbation equations is justified [i.e., terms of $O(k\tilde{\eta})^2$ and higher are neglected]. The mean free-stream velocity U_∞ and the boundary-layer thickness δ are used for normalization.†

The resulting mean flow equations are (see § 2.1 for notation and conventions)

$$-\frac{\partial P}{\partial x^*} + \frac{\partial}{\partial y^*}\left(\frac{1}{Re}\frac{\partial U}{\partial y^*} - \overline{u'v'}\right) = 0, \tag{2.8}$$

$$-\frac{\partial P}{\partial y^*} = \frac{\partial}{\partial y^*}(\overline{v'v'}), \tag{2.9}$$

and, if phase averages are taken before time averages, the differences between phase-averaged and time-averaged equations are the wave perturbation equations, viz.

Continuity equation:

$$\frac{\partial \tilde{u}}{\partial x^*} - f\frac{\partial \tilde{\eta}}{\partial x^*}\frac{\partial U}{\partial y^*} + \frac{\partial \tilde{v}}{\partial y^*} = 0. \tag{2.10}$$

† Our experiment indicates the flow is almost fully developed at the data-taking station; hence, the fully developed assumption is a reasonable approximation. For an almost fully developed flow, the boundary-layer thickness δ is better than the height H as a flow length scale to non-dimensionalize the variables. As a result if it is necessary to let $H \to \infty$, our analysis should still be adequate.

x-momentum equation:

$$\frac{\partial \tilde{u}}{\partial t^*} - f\frac{\partial \tilde{\eta}}{\partial t^*}\frac{\partial U}{\partial y^*} + U\left(\frac{\partial \tilde{u}}{\partial x^*} - f\frac{\partial \tilde{\eta}}{\partial x^*}\frac{\partial U}{\partial y^*}\right) + \tilde{v}\frac{\partial U}{\partial y^*}$$
$$+ \frac{\partial}{\partial x^*}\tilde{r}_{11} - f\frac{\partial \tilde{\eta}}{\partial x^*}\frac{\partial}{\partial y^*}(\overline{u'u'}) + \frac{\partial}{\partial y^*}\tilde{r}_{12} - \frac{\partial f}{\partial y^*}\tilde{\eta}\frac{\partial}{\partial y^*}(\overline{u'v'})$$
$$= -\frac{\partial \tilde{p}}{\partial x^*} + f\frac{\partial \tilde{\eta}}{\partial x^*}\frac{\partial P}{\partial y^*} + \frac{1}{Re}\left[\frac{\partial^2 \tilde{u}}{\partial x^{*2}} - f\frac{\partial^2 \tilde{\eta}}{\partial x^{*2}}\frac{\partial U}{\partial y^*} + \frac{\partial^2 \tilde{u}}{\partial y^{*2}}\right.$$
$$\left. - 2\frac{\partial f}{\partial y^*}\tilde{\eta}\frac{\partial^2 U}{\partial y^{*2}} - \frac{\partial^2 f}{\partial y^{*2}}\tilde{\eta}\frac{\partial U}{\partial y^*}\right]. \quad (2.11)$$

y-momentum equation:

$$\frac{\partial \tilde{v}}{\partial t^*} + U\frac{\partial \tilde{v}}{\partial x^*} + \frac{\partial \tilde{r}_{12}}{\partial x^*} - f\frac{\partial \tilde{\eta}}{\partial x^*}\frac{\partial}{\partial y^*}(\overline{u'v'}) + \frac{\partial \tilde{r}_{22}}{\partial y^*} - \frac{\partial f}{\partial y^*}\tilde{\eta}\frac{\partial}{\partial y^*}(\overline{v'v'})$$
$$= -\frac{\partial \tilde{p}}{\partial y^*} + \frac{\partial f}{\partial y^*}\tilde{\eta}\frac{\partial P}{\partial y^*} + \frac{1}{Re}\left[\frac{\partial^2 \tilde{v}}{\partial x^{*2}} + \frac{\partial^2 \tilde{v}}{\partial y^{*2}}\right]. \quad (2.12)$$

Here $Re = U_\infty \delta/\nu$ is the Reynolds number and

$$\tilde{r}_{ij}(x^*, y^*, t^*) = \langle u_i' u_j' \rangle - \overline{u_i' u_j'} \quad (2.13)$$

are the wave-induced turbulent Reynolds stresses. Also the mean profile $U = U(y^*)$ so that the mean flow is presumed to 'follow' the interface.

The interface boundary conditions for $\tilde{u}$ and $\tilde{v}$ can now be specified. The no slip condition implies that at the interface the air particles have no motion relative to the water, which is assumed to be moving (approximately) with the combined velocity caused by the circular-orbits of deep-water wave motion and by the drift current. Accordingly, we have, to first order (Phillips 1977, p. 95),

$$\left.\begin{aligned} \tilde{u}(x^*, y^*, t^*) &= k(c + U_0)\,\tilde{\eta} \\ \tilde{v}(x^*, y^*, t^*) &= \frac{\partial \tilde{\eta}}{\partial t^*} + U_0\frac{\partial \tilde{\eta}}{\partial x^*} \end{aligned}\right\} \quad \text{at} \quad y^* = 0 \qquad (2.14a, b)$$

where c is the wave celerity and U_0 is the surface drift velocity (which by definition is the time-average of U at $y^* = 0$).

Equations (2.10)–(2.12) are similar to those used by Norris & Reynolds (1975), but with some differences in detail. We emphasize that (*a*) the mean and the wave-induced flow quantities are those measured and decomposed in the transformed wave-following frame and (*b*) in reaching (2.10)–(2.12) we require only ka to be small. This is less restrictive than the limit in a fixed-frame analysis and a typical turbulent flow, whose diffusive layer is considerably thinner than the wave amplitude, can be treated in our analysis. [For a detailed discussion on this see Benjamin (1959), p. 168.]

The terms with $\tilde{\eta}$ in equations (2.10), (2.11) and (2.12) are inhomogeneous terms because they are known if the mean flow and the surface wave fields are prescribed. It is easy to show from control volume analysis that the inhomogeneous terms are produced by the horizontal flow crossing the upper and lower boundaries (which are at constant y^*) of the control volume. The inhomogeneous terms are the consequence of using the non-orthogonal co-ordinate system (x^*, y^*, t^*) which is not aligned with

the Cartesian flow quantities such as u_i and $\overline{u_i'u_j'}$. These inhomogeneous terms can be eliminated from (2.10)–(2.12) by using the following relations,

$$\tilde{u}^*(x^*, y^*, t^*) = \tilde{u}(x^*, y^*, t^*) - f\tilde{\eta}\frac{\partial U}{\partial y^*}, \tag{2.15a}$$

$$\tilde{v}^*(x^*, y^*, t^*) = \tilde{v}(x^*, y^*, t^*), \tag{2.15b}$$

$$\tilde{p}^*(x^*, y^*, t^*) = \tilde{p}(x^*, y^*, t^*) - f\tilde{\eta}\frac{\partial P}{\partial y^*}, \tag{2.15c}$$

$$\tilde{r}_{ij}^*(x^*, y^*, t^*) = \tilde{r}_{ij}(x^*, y^*, t^*) - f\tilde{\eta}\frac{\partial}{\partial y^*}(\overline{u_i'u_j'}), \tag{2.15d}$$

and the mean flow equations (2.8) and (2.9). The resulting equations in terms of $\tilde{u}^*$, $\tilde{v}^*$, $\tilde{p}^*$, and $\tilde{r}_{ij}^*$ in (x^*, y^*, t^*) are identical in form to those obtained by a fixed-frame treatment and perturbation analysis; the same result is obtained for the interface boundary conditions. This indicates that the solutions of the equations for $\tilde{u}^*$, $\tilde{v}^*$, $\tilde{p}^*$, and $\tilde{r}_{ij}^*$ in the (x^*, y^*, t^*) system must be identical to those for $\tilde{u}$, $\tilde{v}$, $\tilde{p}$, and $\tilde{r}_{ij}$ in the (x, y, t) system if the same forms of mean velocity profile and closure relations are used in obtaining the solutions.

It can be shown (see Hsu, Hsu & Street 1977) that the perturbation scheme in a fixed frame analysis is uniformly valid only when

$$a^+/\delta_0^+ \ll 1 \tag{2.16}$$

where $a^+ = au_*/\nu$ is a non-dimensional roughness height for the wave, where u_* is the friction velocity, and $\delta_0^+ = \delta_0 u_*/\nu = U_\infty/u_*$ is the non-dimensional viscous sublayer thickness [$\delta_0 = U_\infty/(\partial U/\partial y^*)_0 = U_\infty \nu/u_*^2$]. When (2.16) is satisfied,

$$\tilde{g}^*(x^*, y^*, t^*)|_{y^*=h} \quad \text{and} \quad \tilde{g}(x, y, t)|_{y=h}$$

can be taken as the same (to second order) and the wave-induced quantities measured in (x^*, y^*, t^*) are related to the wave-induced quantities measured in (x, y, t) by equations (2.15*a*, *b*, *c*, *d*), e.g., $\tilde{u}(x, y, t) = \tilde{u}(x^*, y^*, t^*) - f\tilde{\eta}\,\partial U/\partial y^*$, etc. Accordingly, the differences between the transformed wave-following frame and the fixed frame measurements are clear.

When (2.16) is not satisfied, but the wave slope is still small so that $\tilde{g}^*(x^*, y^*, t^*)$ is still meaningful while $\tilde{g}(x, y, t)$ is not, the fixed-frame analysis actually yields $\tilde{g}^*(x^*, y^*, t^*)$ instead of $\tilde{g}(x, y, t)$ if the results are interpreted to be given in terms of distance above the instantaneous water surface. [We find that our stream function $\tilde{\phi}^*$, defined by $\tilde{u}^* = \partial\tilde{\phi}^*/\partial y^*$ and $\tilde{v}^* = -\partial\tilde{\phi}^*/\partial x^*$, has a role equivalent to $F(\eta)$ in Benjamin (1959).] Condition (2.16) is not satisfied in a laboratory facility, in general, because the wave amplitude has to be maintained large enough to give a significant signal-to-noise ratio. For instance, in this work $u_* = 8{\cdot}56$ cm s^{-1}, $U_\infty = 2{\cdot}4$ m s^{-1} and $a = 2{\cdot}67$ cm; thus, $\delta_0^+ = 28$, $a^+ = 146$, and $a^+/\delta_0^+ = 5{\cdot}24 > 1$. Hence, we conclude that measurements in the fixed-frame cannot be complete and in general are not compatible with attempts to verify model predictions.

According to (2.15*d*), a homogeneous closure model for $\tilde{r}_{ij}(x^*, y^*, t^*)$ will result in

an inhomogeneous closure model for $\tilde{r}_{ij}^*(x^*, y^*, t^*)$. For example, a quasi-laminar model with $\tilde{r}_{ij}(x^*, y^*, t^*) = 0$ in the transformed frame gives

$$\tilde{r}_{ij}^*(x^*, y^*, t^*) = -f\tilde{\eta}\frac{\partial}{\partial y^*}(\overline{u_i' u_j'}). \tag{2.17}$$

If we adopt the closure relations for the mean flow used by Davis (1970), we find that, as $H \to \infty$, (2.17) is identical to Davis' closure relation for $\tilde{r}_{ij}(x, y, t)$. Hence, Davis' (1970) model is the simplest quasi-laminar model in (x^*, y^*, t^*).

The prediction by Davis (1970) was compared to fixed-frame measurements by Stewart (1970) and showed no consistency. Our analysis in the previous subsection indicates that Davis' model, which used the wave-following property of the mean flow suggested by Benjamin (1959) but was applied in the fixed frame, can be adequately tested only by comparison to the quantities $\tilde{g}^*$ measured in (x^*, y^*, t^*). This comparison is made below. However, in view of the importance of the wave-induced turbulent Reynolds stresses, one may anticipate that a non-zero closure for $\tilde{r}_{ij}(x^*, y^*, t^*)$ is essential.

3. Experiments

3.1. *The experimental apparatus and instrumentation*

The channel used for the experiments was described in detail by Hsu (1965) and subsequent investigators at Stanford (see, for example, Bole & Hsu 1969). The wind, water-wave research facility was designed to generate water waves by wind and/or by a mechanical wave generator to facilitate the experimental study of the wave generation problem. The test section is about 20 m long, beginning at the air-flow inlet. The distance H in the air from the mean water level to the channel roof is 0·97 m; the water depth is about 1 m which ensures the 1 Hz mechanically generated water wave used here is a deep water wave. The wave length of this wave was 1·56 m which gives $k = 4{\cdot}03\ \mathrm{m}^{-1}$. The data taking station was located 13 m from the air inlet of the channel.

To measure the flow in the transformed wave-following frame, the wave-follower system developed by Yu, Hsu & Street (1971) was modified and used as the primary instrument. The wave-follower system is controlled to allow one to set the mean elevation accurately ($\pm 0{\cdot}25$ mm) and to fix the oscillation amplitude, using the signal output of a fixed wave-height gauge as input, such that the probes move vertically so y^* = constant. The vertical motion range of the wave-follower is about 15 cm; thus for a 2·67 cm amplitude water wave only about 9 cm of the boundary layer can be traversed. This traverse range is approximately one third of the boundary-layer thickness. The vertical traverse range was extended, with the aid of a wave-follower elevator, to cover the whole boundary layer. The arrangement of the components and the measuring probes is shown in figure 1. To correct for the phase lag of the wave-follower system the wave-height gauge was installed approximately 4·0 cm upstream of the velocity probes, which were attached to the lower end of the wave-follower.

The wave-height gauge that measured the elevation of the instantaneous water surface, was a capacitance type (Colonell 1966). The accuracy of the gauge calibration in static and dynamic tests was $\pm 0{\cdot}25$ mm.

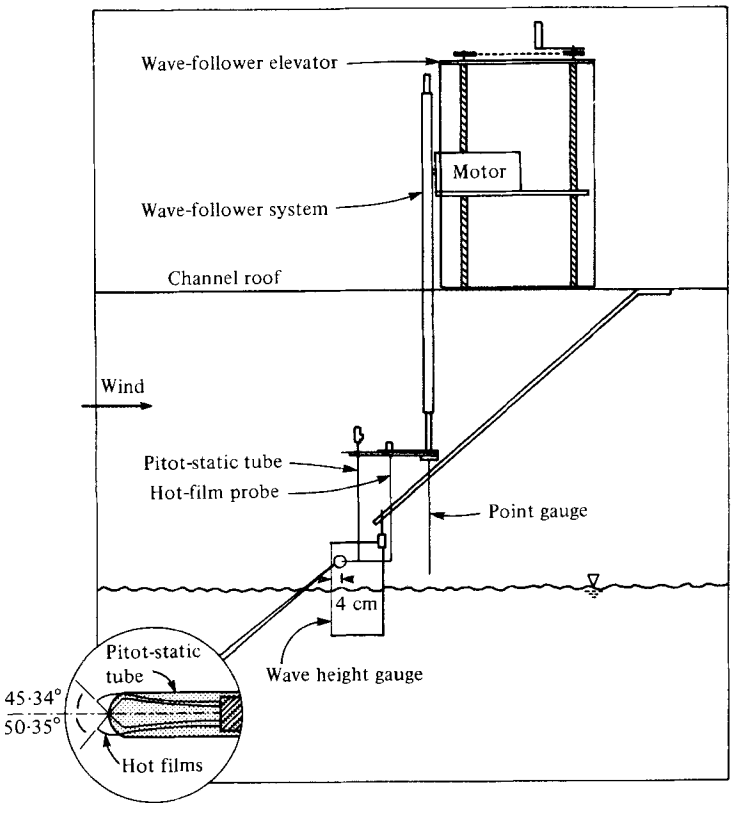

FIGURE 1. Probe configurations.

A Pitot-static tube was used to cross check the mean velocity obtained from hot-film probes and to calibrate them. The output from the Pitot-static tube was taken to a Pace differential transducer (Model P90D) which was calibrated against a micro-manometer, with resolution of 0·0006 cm of silicone oil (specific gravity 0·82).

The hot-film probe used to measure the velocity fields was a TSI Model 1241-20. The orientation angles of the films relative to the probe centre-line, which were measured with the aid of an optical comparator, are shown in figure 1. Each film was operated in a constant temperature mode. The hot-film probe was calibrated *in situ* immediately prior to data taking. The misalignment of the probe was determined by recalibrating the probe after 180° rotation about the probe axis; the misalignment was less than 1°. The uncertainty in the hot-film probe calibration was mainly caused by the uncertainty in the Pitot-static tube output and was approximately 3 %. This was confirmed by oscillating the hot-film probe in the free stream where the output should correlate closely with the oscillation velocities. No spurious errors, due for example to mount resonance, were observed.

3.2. *Data acquisition and reduction*

The wave height and velocity data were taken simultaneously and recorded by a data acquisition-reduction system. The system consists of an HP2100A computer, analog-to-digital converter, nine-track magnetic tape drive and peripheral input–

output devices (Takeuchi & Mogel 1975). All the signals were zero-suppressed, amplified and low-pass filtered at 500 Hz to fulfil the Nyquist criterion as samples were taken every 0·001 s for 3 min. The air and water flows were permitted to settle into statistical equilibrium over a 1 hour period prior to taking data. The sampled data were stored on digital magnetic tape.

All data were taken at the same mean free-stream velocity of 2·4 m s^{-1} and with mechanically-generated water waves of 1 Hz frequency and 2·67 cm amplitude. Velocity data were taken at 18 elevations ranging from 1·6 cm to about 39 cm above the interface.

The time and phase averages given by equations (2.1) and (2.2) are the main techniques used for data reduction. The wave component $\tilde{g}$ is then determined by equation (2.3). Because $\tilde{g}$ contains all the harmonics, cross-spectral and auto-spectral analyses for $\tilde{g}$ using $\tilde{\eta}$ as a reference were performed by fast Fourier transformation (FFT) to determine the amplitudes and the phases of each harmonic. The resultant amplitudes showed that the contribution of harmonics is less than 10 % of the fundamental mode for all reduced quantities. Hence, a linear analysis for the wave perturbed fields is feasible.

Special attention was given to the calculations of $\tilde{v}(x^*, y^*, t^*)$ and $\tilde{r}_{ij}(x^*, y^*, t^*)$. The velocity sensors measured the velocity of a fluid element relative to the probe, which is not consistent with the Cartesian velocity described in the transformed coordinate system. Since the probe moves with a vertical velocity $f\,\partial\tilde{\eta}/\partial t^*$, we have

$$\tilde{u}_m(x^*, y^*, t^*) = \tilde{u}(x^*, y^*, t^*), \tag{3.1a}$$

$$\tilde{v}_m(x^*, y^*, t^*) = \tilde{v}(x^*, y^*, t^*) - f\frac{\partial\tilde{\eta}}{\partial t^*}, \tag{3.1b}$$

where $\tilde{u}_m$ and $\tilde{v}_m$ are the wave-induced velocities measured by the probe. To obtain $\tilde{r}_{ij}$, $\langle u_i' u_j' \rangle$ was first deduced according to the relation

$$\langle u_i' u_j' \rangle = \langle (\tilde{u}_{mi} + u_i')(\tilde{u}_{mj} + u_j') \rangle - \tilde{u}_{mi}\tilde{u}_{mj}, \tag{3.2}$$

where $\tilde{u}_{m1} = \tilde{u}_m$ and $\tilde{u}_{m2} = \tilde{v}_m$. Then $\overline{u_i' u_j'}$ was obtained by averaging $\langle u_i' u_j' \rangle$ over the wave period and $\tilde{r}_{ij}$ was in turn calculated from equation (2.13).

For the raw data the time between samples is 0·001 s, yielding a frequency resolution of 0·976 Hz for spectral estimates. This resolution is inadequate for the study of the effects of a 1 Hz mechanically generated wave. However, we can treat the phase-averaged data for a quantity $\tilde{g}$ as periodic and string together enough cyclic repetitions of the data to create, effectively, a new and longer data set. This longer set is digitally low-pass filtered and then re-sampled at a prime number multiple of the original time increment, i.e. every 0·023 s. For a 1024 point FFT and 1 Hz waves, one needs just over 23 periods of wave data. The result is a frequency resolution of about 0·04 Hz and the 512 spectral points lie in the range $0{\cdot}04 < f < 22$ Hz. The low-pass digital filtering at an appropriate cut-off frequency prevents aliasing error due to the re-sampling. The identical low-pass digital filtering and re-sampling processes were applied to $\tilde{\eta}$ to eliminate the effect of phase change by the filter. The changes in the amplitude of $\tilde{g}$ by the digital filter were also corrected from the known filter characteristics. The low-pass digital filter is a recursive filter given by Bendat & Piersol (1971, p. 297). Details of the fast Fourier transform procedure and of the spectral analysis can also be found in Bendat & Piersol (1971, cha. 9).

4. Experimental results

4.1. *Format of presentation*

The flow quantities are generally presented in profile distributions as a function of y^*. The profiles are usually in non-dimensional form; typically U_∞ and U_∞^2 are used to normalize the velocities and the Reynolds stresses, respectively, and the ordinates y^* are normalized by k. However, when interpretation in wall co-ordinates is required, the friction velocity u_* and the viscous length scale ν/u_* are used for normalization. The wave-induced quantity $\tilde{g}$ is generally expressed as

$$\begin{aligned}\tilde{g}(x^*, y^*, t^*) &= \tfrac{1}{2}[\hat{g}(y^*)\exp[i(kx^* - \omega t^*)] + \text{conjugate}] + \text{harmonics} \\ &= |\hat{g}(y^*)|\cos(kx^* - \omega t^* + \theta_{\tilde{g}}) + \text{harmonics}, \end{aligned} \tag{4.1}$$

where $|\hat{g}(y^*)|$ is the amplitude and $\theta_{\tilde{g}}$ is the phase lag angle of the fundamental mode. The phase lag is with respect to time using $\tilde{\eta}$ as a reference. In this study, the wave perturbation quantity can be approximated by its fundamental mode without changing overall conclusions, because as noted above the harmonics are relatively weak.

4.2. *Water-wave field and surface condition*

A typical result for the phase average of the mechanically generated water wave is shown in figure 2, together with the phase-average results of $\tilde{u}$, $\tilde{v}$, and $\tilde{r}_{ij}$ for $U_\infty = 2{\cdot}4$ m s^{-1} and $y^* = 1{\cdot}6$ cm. Strong correlations among $\tilde{\eta}$, $\tilde{u}$, $\tilde{v}$, and $\tilde{r}_{ij}$ are seen in figure 2. From auto-spectral analysis, the harmonics in $\tilde{\eta}$ are less than 5 % of the fundamental mode and are negligible. Here $ka = 0{\cdot}107$, corresponding to $a = 2{\cdot}67$ cm.

For $U_\infty = 2{\cdot}4$ m s^{-1}, the ripples η' riding on the mechanically generated water waves are small but visible. The randomness of the ripples results in $\overline{\eta'} = \langle \eta' \rangle = 0$; however, the mean square $\overline{\eta'^2}$ is non-zero and represents the square of mean surface roughness on the mechanically generated water waves. The roughness parameter $z^+ = z_0 u_*/\nu = 4{\cdot}95$ where $z_0 = \overline{\eta'^2}^{\frac{1}{2}}$ is the mean roughness of the ripples and is approximately equal to 0·09 cm for this study. Hence, we conclude that the surface condition is aerodynamically smooth.

4.3. *Mean flow fields*

(*a*) *Mean velocity profile.* The mean horizontal velocity profile obtained in this experiment is typical of that for a turbulent boundary-layer flow. There is a log-linear profile near the interface and a wake characteristic near the free stream. We first used

$$u^+ = k_0^{-1} \ln y^+ + C, \tag{4.2}$$

where $u^+ = U/u_*$ and $y^+ = y^* u_*/\nu$ are the wall co-ordinates and k_0 is von Kármán's constant (assumed to be 0·40), to fit the lower portion of the mean velocity profile. The friction velocity u_* found is approximately 30 % greater than that calculated from direct measurement, i.e. from $u_*^2 = -\overline{u'v'}$. The results for u_* also depend on the number of points in the linear portion of the profile used for curve-fitting, the variation being as large as 15 %. Furthermore, all the y^+ values for the data points are greater than 100, which is contrary to the argument that the log-linear profile exists only for $30 < y^+ < 70$. Hence, the simple log-linear curve-fit was discarded in favour of the better results produced by the use of the profile of the 'law of the wake'

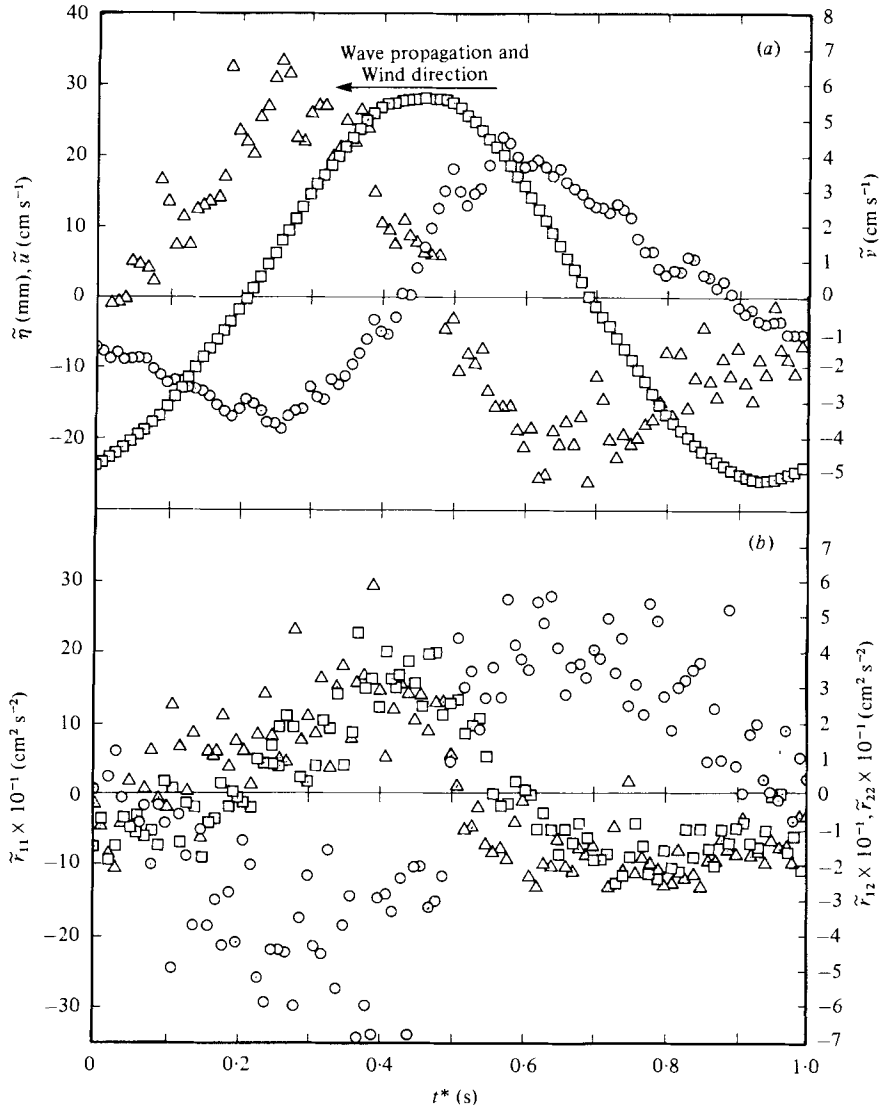

FIGURE 2. Phase-averaged results for $\tilde{\eta}$, $\tilde{u}_i$ and $\tilde{r}_{ij}$ at $y^* = 1{\cdot}604$ cm, $U_\infty = 2{\cdot}4$ m s^{-1}. (*a*) ⊡, $\tilde{\eta}$; ○, $\tilde{u}$; △, $\tilde{v}$. (*b*) ⊡, $\tilde{r}_{11}$; ○, $\tilde{r}_{12}$; △, $\tilde{r}_{22}$. Note that $\tilde{r}_{11}$ and $\tilde{r}_{22}$ are almost in phase and are almost in 90° lead to $\tilde{r}_{12}$.

(Coles 1956), which can be written as

$$\frac{U_\infty - U}{u_*} = -\frac{1}{k_0}\ln\frac{y^*}{\delta} + \frac{W_c}{k_0}\left[2 - W\left(\frac{y^*}{\delta}\right)\right], \tag{4.3}$$

where W is the wake function and W_c is the wake parameter. The wake function W can be approximated by (Hinze 1975)

$$W(y^*/\delta) = 1 - \cos(\pi y^*/\delta). \tag{4.4}$$

Equation (4.3) can be written as

$$u^+ = \frac{1}{k_0}\ln y^+ + C + \frac{W_c}{k_0}\left[1 - \cos\left(\frac{\pi y^+}{\delta^+}\right)\right], \tag{4.5}$$

Profile parameters (results of curve fitting)						Direct measurement	Difference
U_∞ (cm s^{-1})	δ (cm)	W_c	C	δ^+	u_* (cm s^{-1})	u_* (cm s^{-1})	$\frac{\Delta u_*}{u_*} \times 100\,\%$
239·4	23·50	0·3240	8·619	1267	8·520	8·561	0·48

TABLE 1. Parameters for mean velocity profiles and comparisons of the friction velocity. For flow over a mechanically-generated water-wave of frequency 1 Hz and amplitude 2·67 cm; the wave celerity $c = 1{\cdot}56$ m s^{-1} and the wave slope $ka = 0{\cdot}107$. Wind/wave coupling parameter: $c/u_* = 18{\cdot}2$, $U_\infty/c = 1{\cdot}54$.

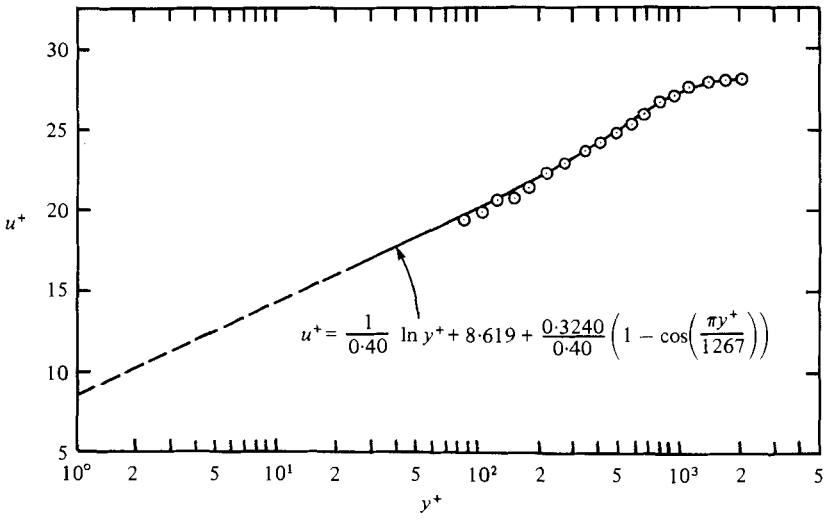

FIGURE 3. Mean horizontal velocity profiles in wall co-ordinates; the profile parameters U_∞, u_* δ^+ and W_c are given in table 1. ○, experimental results; ——, curve-fit results.

which asymptotically matches (4.2) as $y^+ \to 0$ with the matching condition

$$C = u_\infty^+ - \frac{1}{k_0} \ln \delta^+ - 2\frac{W_c}{k_0}, \tag{4.6}$$

where $u_\infty^+ = U_\infty/u_*$ and $\delta^+ = \delta u_*/\nu$. Note that equation (4.5) applies in the region from $y^+ = 30$ to the free stream.

Figure 3 shows the comparison of the data to the results of curve-fitting by the least-square method. The agreements are excellent. The profile parameters are given in table 1. The comparison of u_* between the results of curve-fitting and of direct measurement gives a difference of 0·48 % as shown in table 1. Note that use of the law of the wake is very much better than use of the normally used log-linear profile technique. The parameters U_∞/c, u_*/U_∞, c/u_*, and $U_\infty\delta/\nu$ which characterize the mean flow were 1·54, 0·0359, 18·2, and 35700 respectively.

(*b*) *Mean Reynolds stresses and turbulent intensity.* Figure 4 shows the distributions of the turbulent Reynolds stresses $\overline{u_i' u_j'}$. The typical behaviour of these distributions is the same as those measured in flow over a flat plate by Klebanoff (1955) (see also

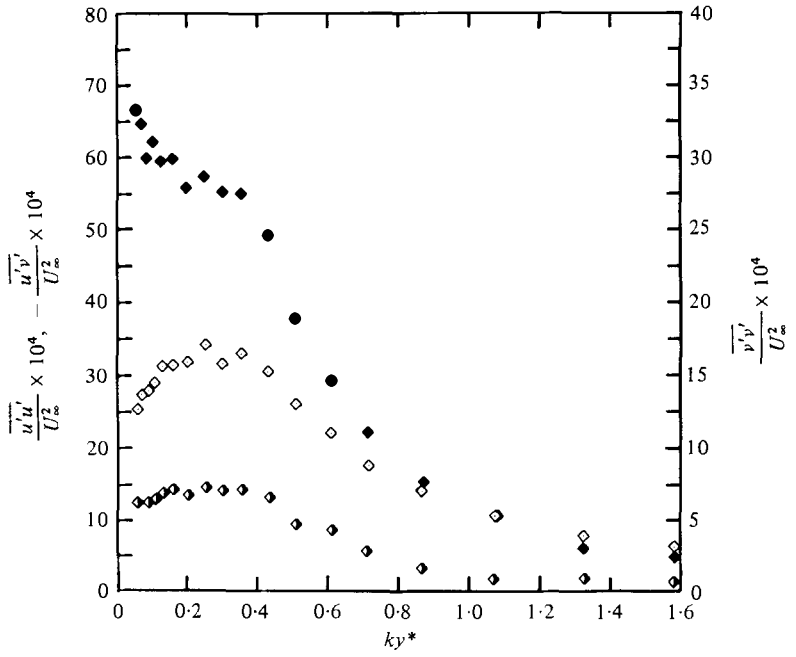

FIGURE 4. Distributions of mean tubulent Reynolds stresses; $U_\infty = 2{\cdot}4$ m s^{-1}.
◆, $\overline{u'u'}/U_\infty^2$; ◈, $-\overline{u'v'}/U_\infty^2$; ◇, $\overline{v'v'}/U_\infty^2$.

Schlichting 1968). An almost constant shear layer is observed in the lower portion of the $-\overline{u'v'}$ profile. The turbulent shear stress outside the viscous sublayer is

$$-\overline{u'v'}/U_\infty^2 = (u_*/U_\infty)^2 \simeq 0{\cdot}0013.$$

For a typical turbulent boundary layer flow over smooth flat plate, we find from figure 21.7 in Schlichting (1968, p. 611) that $-\overline{u'v'}/U_\infty^2 = 0{\cdot}0017$ for

$$Re_x = U_\infty x/\nu \simeq 2{\cdot}0 \times 10^6$$

based on the fetch of the data-taking station. The lower value in the shear stress for the interface flow may be due to the influence of the developing drift current at the interface which results in a partial release of the shear stress (see additional discussion in § 5).

4.4. *Wave perturbation fields*

(*a*) *Wave perturbation velocities.* A typical result for $\tilde{u}$ and $\tilde{v}$ obtained by phase averaging is shown in figure 2. The deviation of $\tilde{u}$ and $\tilde{v}$ from the nearly sinusoidal $\tilde{\eta}$ as indicated suggests a relatively higher nonlinearity in the wave-induced flow. This nonlinear effect may result from the nonlinear advection of the air flow. However, the spectral analysis of $\tilde{u}$ and $\tilde{v}$ indicates that the magnitudes of the harmonics are still less than 10 % of those of the fundamental modes and are negligible.

Figures 5 and 6 show the amplitude and the phase lag versus ky^* for $\tilde{u}$ and $\tilde{v}$, respectively. Near the interface, but outside the viscous sublayer, the magnitude of $|\hat{u}|$ is nearly one order greater than that of $|\hat{v}|$; they tend to be of the same order away

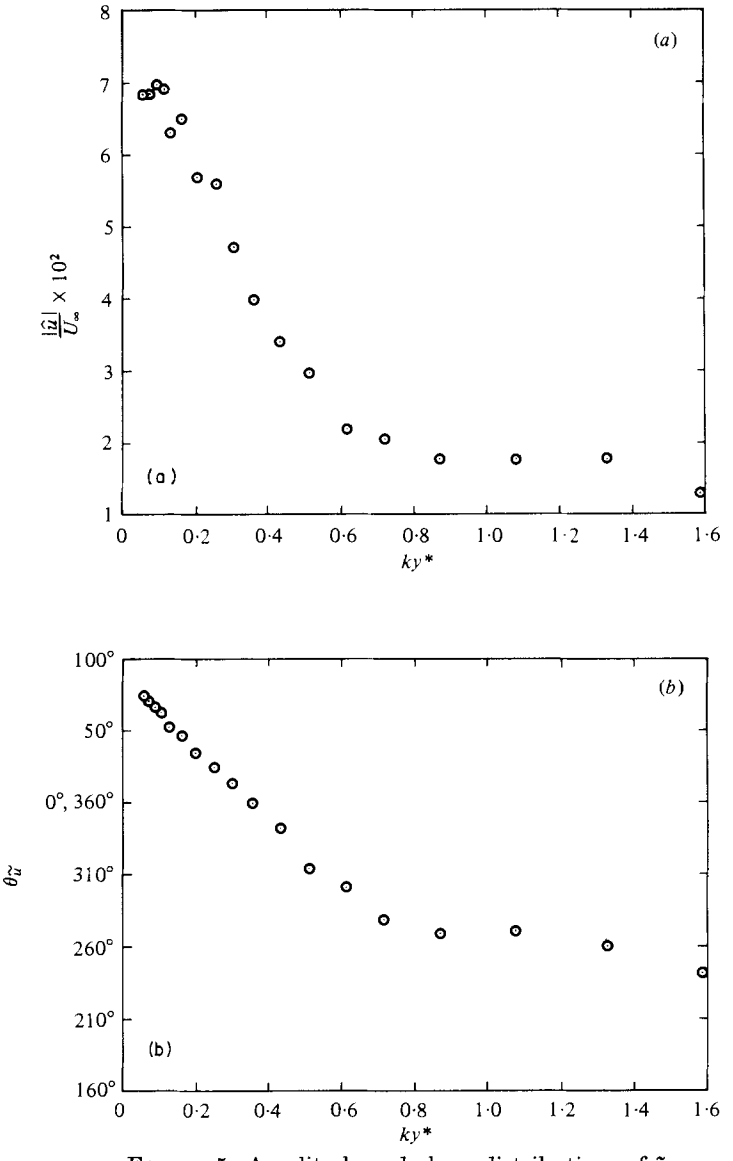

FIGURE 5. Amplitude and phase distributions of $\tilde{u}$.

from the interface. This suggests that, close to the interface where the mean flow vorticity and the turbulent intensity are high, the wave perturbation field strongly depends on the shear flow effect and the turbulent mixing. Away from the interface, the wave perturbation field behaves similar to that in an inviscid flow with constant mean velocity. Hence, the exponential decay character is predominant in the free stream. This is also evidenced by the phase relation between $\theta_{\tilde{u}}$ and $\theta_{\tilde{v}}$, that is, near the free stream, there is an almost constant 90° difference and, near the interface, a 180° difference is observed.

If the drift current at the interface is assumed to be 3 % of U_∞ (Wu 1968), the inter-

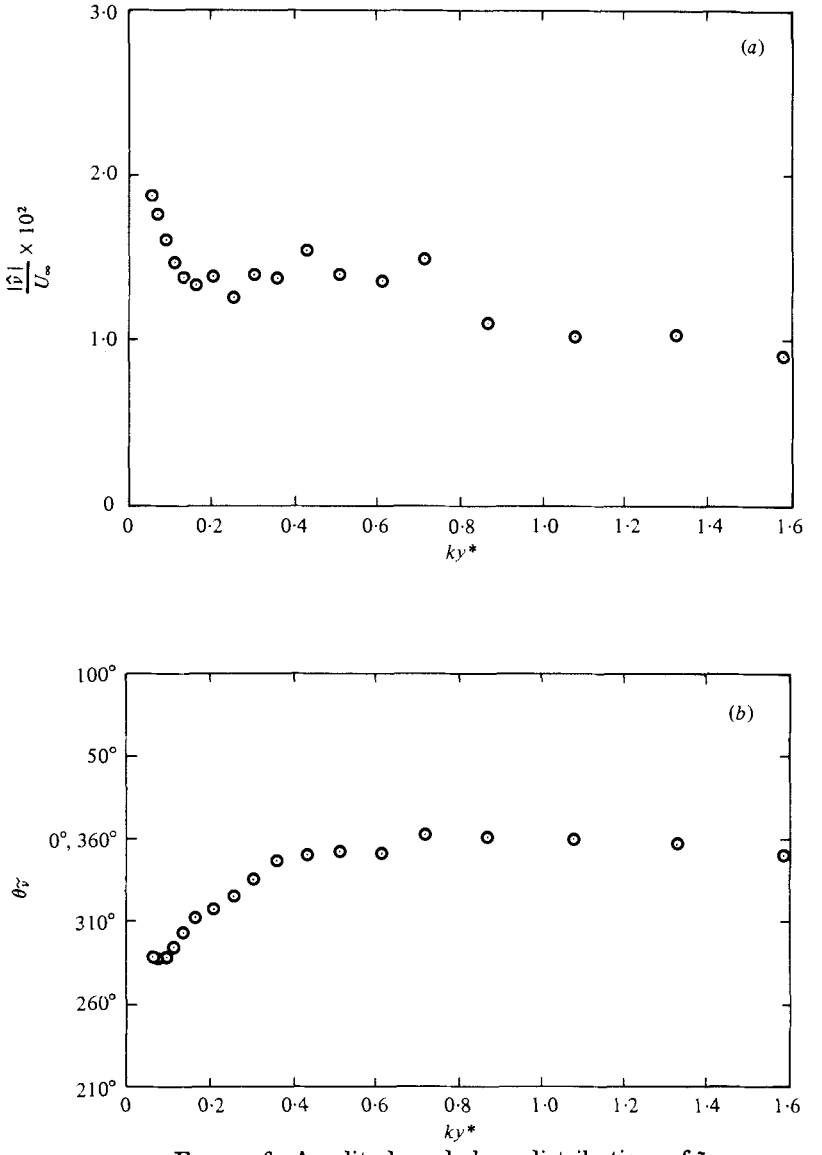

FIGURE 6. Amplitude and phase distributions of $\tilde{v}$.

face boundary condition gives $|\hat{v}|/U_\infty \times 10^2 = 6{\cdot}67$ and $\theta_{\tilde{v}} = 270°$ at $y^* = 0$. The measured sharp increase in $|\hat{v}|$ and the measured phase $\theta_{\tilde{v}}$ approaching 270° as $y^* \to 0$, as shown in figure 6, seem to verify the interface boundary condition.

(*b*) *Wave-associated Reynolds stress.* The distribution of $-\overline{\tilde{u}\tilde{v}}$ is shown in figure 7. When the harmonic modes of $\tilde{u}$ and $\tilde{v}$ are relatively weak compared to the fundamental mode, the wave-associated Reynolds stress $-\overline{\tilde{u}\tilde{v}}$ can be approximated by

$$-\tfrac{1}{2}|\hat{u}|\,|\hat{v}|\cos(\theta_{\tilde{u}} - \theta_{\tilde{v}}).$$

This approximation by the fundamental mode (not shown in figure 7) differs by less

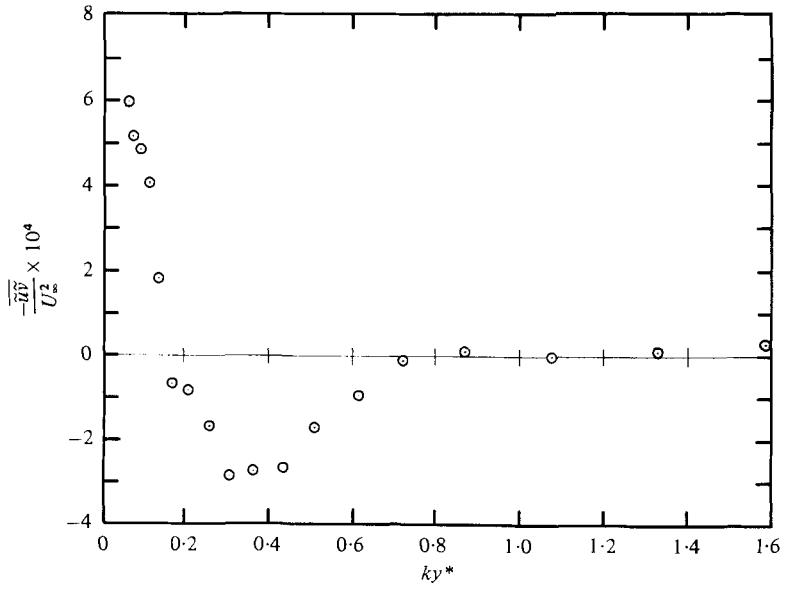

FIGURE 7. Distributions of $-\tilde{u}\tilde{v}$.

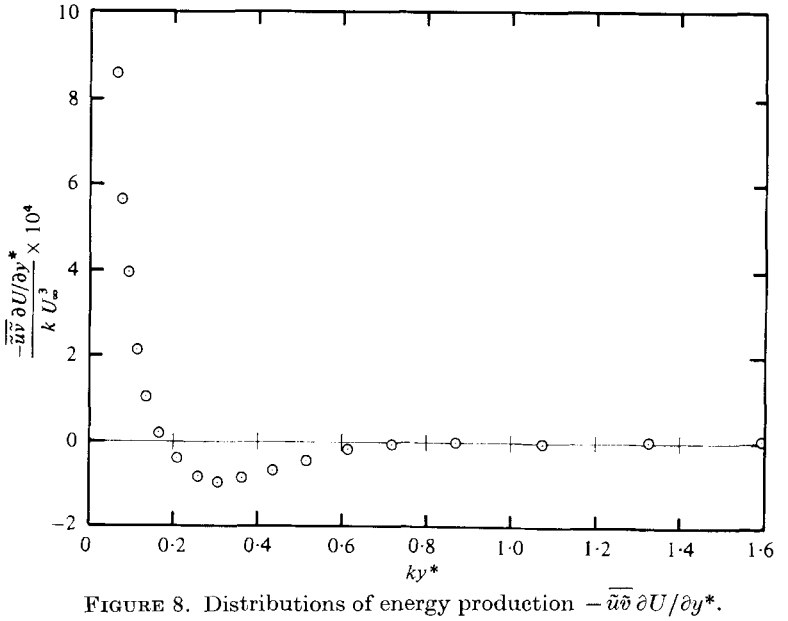

FIGURE 8. Distributions of energy production $-\tilde{u}\tilde{v}\,\partial U/\partial y^*$.

than 5 % from the measured results. The interesting features in $-\tilde{u}\tilde{v}$ are the high positive value comparable to $-\overline{u'v'}$ near the interface, the drastic decrease to a negative minimum as y^* increases and the recovery to a zero value in the free stream. The variation in $-\tilde{u}\tilde{v}$ is continuous and is in contrast to the prediction based on the inviscid theory of Miles (1957). Kendall (1970) observed similar behaviour; however,

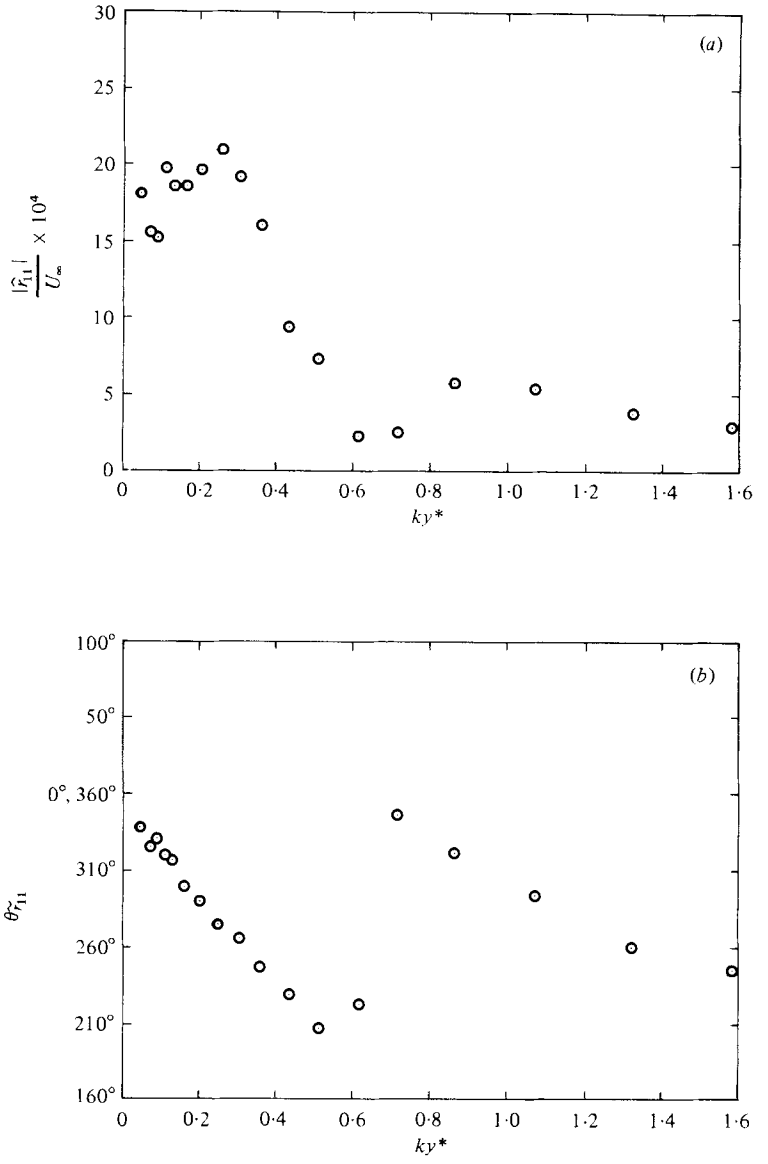

FIGURE 9. Amplitude and phase distributions of $\tilde{r}_{11}$.

his measurements were not close enough to the wave surface to obtain the positive value of $-\overline{\tilde{u}\tilde{v}}$.

The wave-associated Reynolds stress is significant not only in transferring momentum and energy from wind to waves in the wave-generation process, but also in transferring energy from the mean flow to the wave perturbation field. The rate of energy transfer from the mean flow to the wave perturbation field is given by

$$-\overline{\tilde{u}\tilde{v}}\,\partial U/\partial y^*.$$

Because $\partial U/\partial y^* > 0$ in the boundary layer as shown in figure 3, the energy transfer

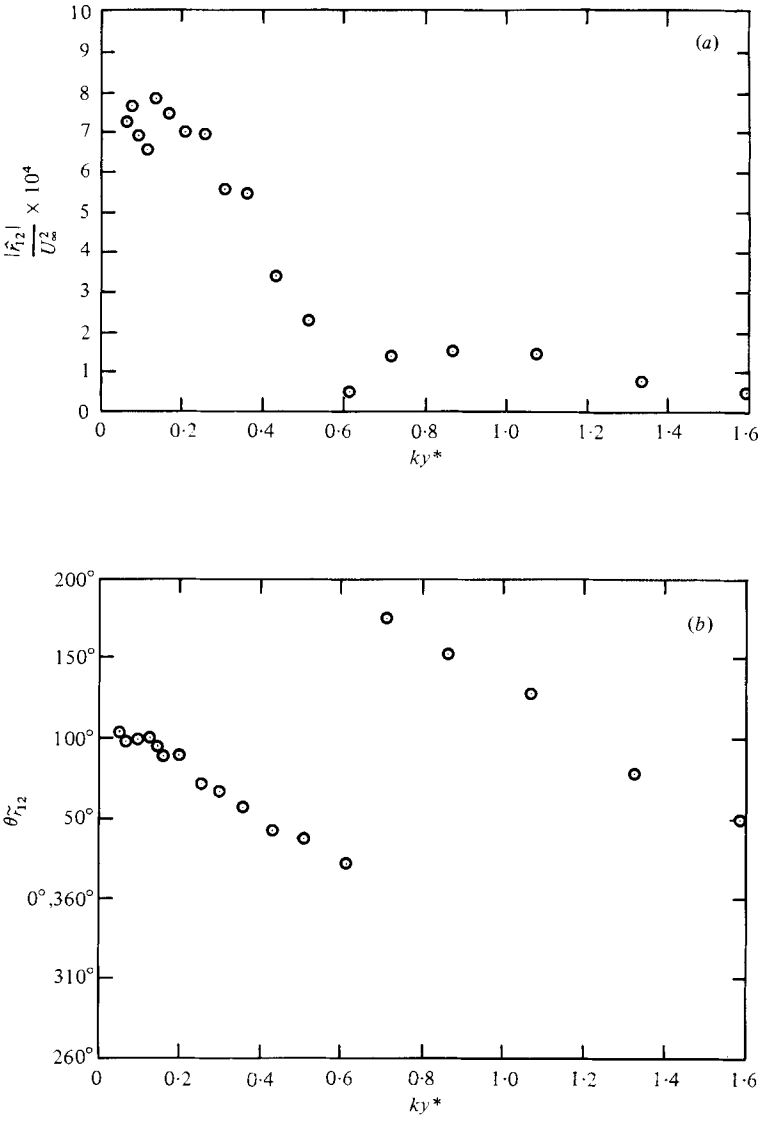

FIGURE 10. Amplitude and phase distributions of $\tilde{r}_{12}$.

rate is negative (from the wave perturbation field to the mean flow) in the upper portion of the boundary layer ($ky^* > 0{\cdot}18$) and is positive (from the mean flow to the wave perturbation field) in the lower portion ($0 < ky^* < 0{\cdot}18$) (see figure 8). The energy production $-\overline{\tilde{u}\tilde{v}}\,\partial U/\partial y^*$ is confined to the boundary layer and is concentrated near the interface.

(c) *Wave-induced turbulent Reynolds stresses.* The phase-average results for $\tilde{r}_{ij}$ at $y^* = 1{\cdot}6$ cm are shown in figure 2. The oscillations $\tilde{r}_{11}$ and $\tilde{r}_{22}$ are coherent and almost in phase. Thus, the oscillatory turbulent intensity $\tilde{q}_0^2 = \tilde{r}_{11} + \tilde{r}_{22}$ is also almost in phase with $\tilde{r}_{11}$ and $\tilde{r}_{22}$. Turbulence is enhanced on the leeward side of the water wave and is reduced on the windward side. The oscillatory shear stress $\tilde{r}_{12}$ shown in figure 2

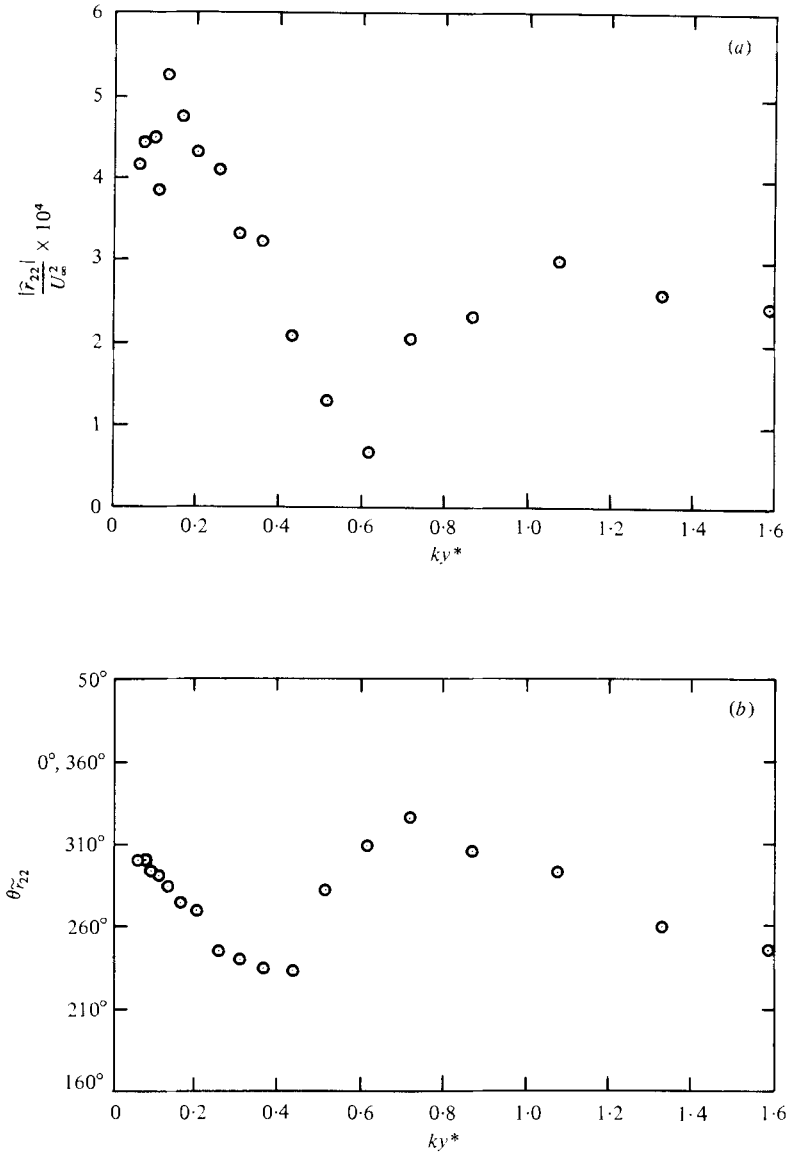

FIGURE 11. Amplitude and phase distributions of $\tilde{r}_{22}$.

indicates that the turbulent Reynolds stress $-\langle u'v' \rangle$ is relatively high on the leeward side and relatively low on the windward side of the mechanically generated water wave. The consistency in the variations of $\hat{r}_{12}$ and $\tilde{q}_0^2$ is expected because higher turbulent intensity usually results in higher turbulent Reynolds stress, although their peaks are not necessarily matched.

The distributions of amplitudes $|\tilde{r}_{ij}|$ and phases $\theta_{\tilde{r}_{ij}}$ are given in figures 9, 10 and 11. The amplitudes $|\hat{r}_{ij}|$ are large near the interface and decrease as y^* increases. They all decrease to a 'minimum' at $ky^* = 0{\cdot}6$ and finally tend to zero in the free stream. We interpret the value of the 'minimum' as zero because there is a phase jump of 180°

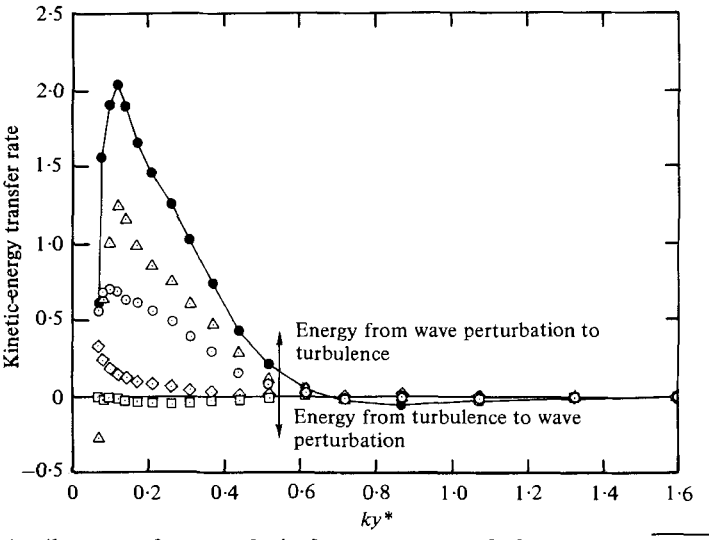

FIGURE 12. Distributions of energy drain from wave to turbulence. ○, $-\overline{\tilde{r}_{11}(\partial\tilde{u}/\partial x^*)} \times 10^4/kU_\infty^3$, (1); △, $-\overline{\tilde{r}_{12}(\partial\tilde{u}/\partial y^*)} \times 10^4/kU_\infty^3$, (2); □, $-\overline{\tilde{r}_{12}(\partial\tilde{v}/\partial x^*)} \times 10^4/kU_\infty^3$, (3); ◇, $-\overline{\tilde{r}_{22}(\partial\tilde{v}/\partial y^*)} \times 10^4/kU_\infty^3$, (4); —●—, net energy drain, (1) + (2) + (3) + (4).

at $ky^* = 0{\cdot}6$ in the $\theta_{\tilde{r}_{ij}}$ profiles. The phase jump of 180° means that the oscillatory turbulent Reynolds stresses just above $ky^* = 0{\cdot}6$ act in the opposite direction to those stresses just below. In comparison among the phase distributions of $\theta_{\tilde{r}_{ij}}$, we find $\tilde{r}_{11}$, $\tilde{r}_{22}$, and then $\tilde{q}_0^2$ have almost the same phase distribution. However, $\tilde{r}_{12}$ has an approximately constant phase difference of 90° compared to $\tilde{r}_{11}$ and $\tilde{r}_{12}$ throughout the boundary layer. We also find $\tilde{u}$ lags $\tilde{r}_{11}$ and $\tilde{r}_{22}$ by approximately 90° for $ky^* < 0{\cdot}6$. This suggests the existence of an eddy-viscosity relation between $\tilde{u}_i$ and $\tilde{r}_{ij}$. An eddy-viscosity closure has been constructed based on these experimental results (see Hsu *et al.* 1977) and is now under test. The results will be reported in a subsequent paper.

Gent & Taylor (1976) used an isotropic eddy viscosity model to calculate the interface flow in a curvilinear co-ordinate system under finite-amplitude wave conditions. The ranges of c/u_* and ka in their study are $4 \leqslant c/u_* \leqslant 20$ and $0{\cdot}01 \leqslant ka \leqslant 0{\cdot}314$ which cover those of our experiment. They predicted that the amplitudes of the induced turbulent Reynolds stresses would have double-peak profiles and that the phase distributions of the induced turbulent Reynolds stresses shift 180° in the downstream direction through the boundary layer. However, their model also predicted that near the interface the maximum turbulent intensity and the maximum turbulent shear stress occur windward of (or behind) the wave crests. For instance, we find from their table 3 that the maximum stress occurs 148° behind the wave crest when $c/u_* = 18$ and $ka = 0{\cdot}157$. This is contrary to our observation which gives the maximum stress at 80° forward of the wave crest. The phase jump of 180° at $ky^* = 0{\cdot}6$ in $\theta_{\tilde{r}_{ij}}$ again was not predicted by their model. The discrepancy may be due to the difference in the surface condition; the surface they assumed is rough while that which we observed is aerodynamically smooth. Neglecting the viscous stress at $y^* = 0$ in their model requires that the eddy viscosity $k_0 z_0 u_*$ be considerably larger than ν say $k_0 z_0 u_*/\nu \geqslant 10$. Consequently, their predictions for $\ln kz_0 = -8$ are only

applicable if $(\omega/2\pi)^3 \leqslant 0{\cdot}32\,(u_*/c)$. This condition is apparently not satisfied by our experiment.

Consideration is now given to the energy exchange in the wave–turbulence interaction. The energy drain from the wave perturbation field to the background turbulent field is given by $-\overline{\tilde{r}_{ij}\,\partial\tilde{u}_i/\partial x_j^*}$. The profiles of $|\hat{u}_i|$, $\theta_{\tilde{u}_i}$, $|\hat{r}_{ij}|$ and $\theta_{\tilde{r}_{ij}}$ shown in figures 5, 6, 9, 10 and 11 were used for calculating the energy drain. The results of the calculation are shown in figure 12. The horizontal stress–strain correlation $-\overline{\tilde{r}_{12}\,\partial\tilde{u}/\partial y^*}$ contributes dominantly to the energy drain near the interface. A drastic change in the energy drain is observed near the interface. The net energy drain indicated by the line segments in figure 12 shows that for $ky^* < 0{\cdot}68$ the wave-induced turbulent Reynolds stresses convert the kinetic energy of the wave perturbation into background turbulence. For $ky^* > 0{\cdot}68$ the energy is transferred from the turbulence to the wave perturbation. The amount of the energy drawn from the wave perturbation field to the turbulence in the lower portion of the boundary layer is much larger than the amount of the energy given to the wave perturbation field from the turbulence near the free stream.

Liu & Merkine (1976) studied the interactions between a wave-like large-scale structure and fine-grained turbulence in a free shear flow. Their prediction of the wave–turbulence energy transfer (figure 3 in their paper) resembles our observations. They showed that the horizontal stress–strain correlation is predominant. However, their predicted total transfer is uniformly from the wave field (large-scale) to the turbulent field (fine-grained turbulence). Our results are related to a boundary-layer flow where there are interactions between the large-scale turbulence and a wave; this may cause the difference between our results and their predictions. In general, however, our observations and their predictions seem to be consistent.

5. Discussion

Discussions were given in § 4 for specific flow quantities. In this section we will discuss the general aspects of our measured results and use them to comment on some controversies between the previous hypotheses and measured results concerning interface flow structure and wave-generation theory.

5.1. *Mean flow structure*

The main controversy about the mean flow is: (*a*) Is the mean flow over the wave, to the first approximation, similar to that of a boundary layer over curved surfaces, so that it can be measured as a function of $y - e^{-ky}\tilde{\eta}$, as pointed out by Benjamin (1959), or (*b*) is the flow representable as fixed profiles in the Cartesian co-ordinate system? From this study in which measurements were made in y^* co-ordinates, the mean velocity has a wake log-linear profile which holds in the vicinity of the interface (and in particular in that section below the wave crests). The measured turbulent Reynolds stresses $\overline{u_i' u_j'}$ also have a structure similar to that observed by others in flat, solid-boundary channels. This suggests that the interface flow characteristics are dependent on the instantaneous height above the water surface consistent with Benjamin's suggestion and are not easily represented in terms of the height above the mean water level. Stewart (1970) measured the velocity profiles over smooth water surfaces and over a 1·96 Hz mechanically generated water wave under a low wind condition (similar to this study). He also confirmed the wave-following property of the mean

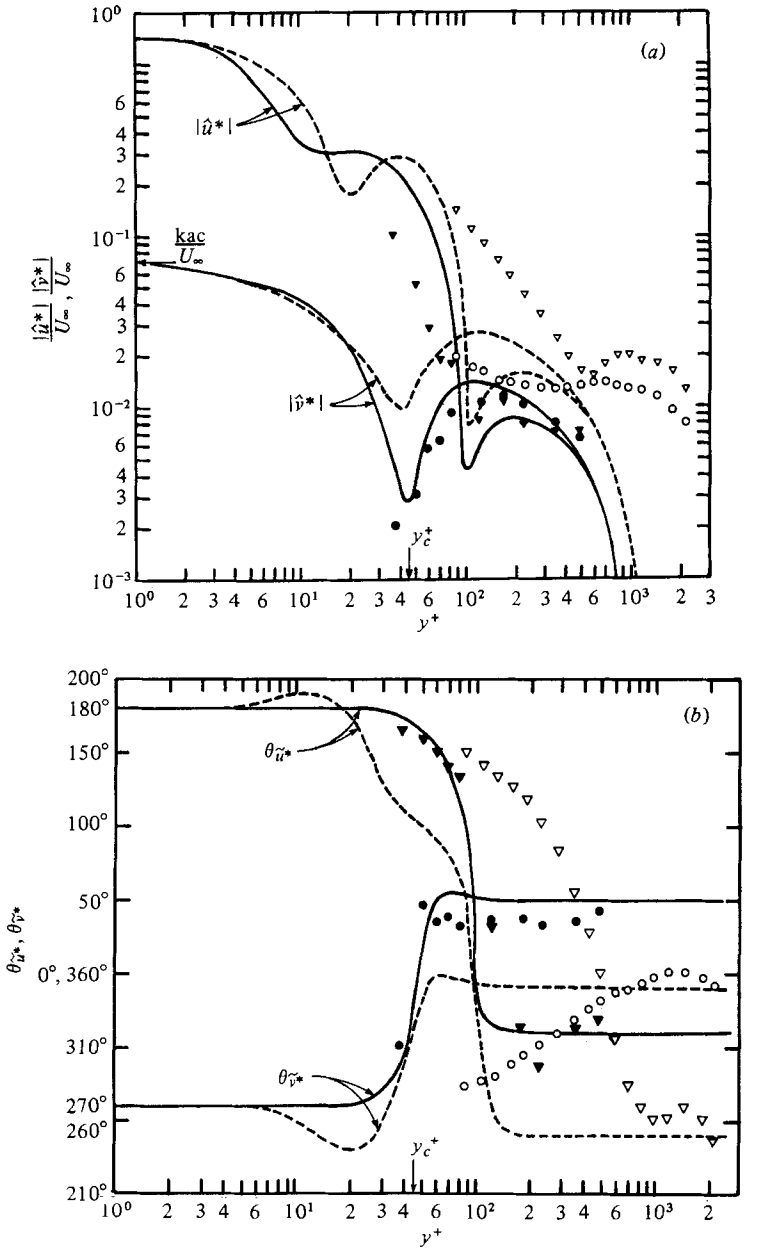

FIGURE 13. (*a*) Amplitude distributions and (*b*) phase distributions of $\tilde{u}^*$ and $\tilde{v}^*$ compared with the measurements of Stewart (1970) and the prediction of Davis (1970). This experiment: ▽, $|\hat{u}^*|$ or θ_{u^*}; ○, $|\hat{v}^*|$ or θ_{v^*}. Stewart's data: ▼, $|\hat{u}^*|$ or θ_{u^*}; ●, $|\hat{v}^*|$ or θ_{v^*}; Davis' predictions: – – –, model *A*; ——, model *B*.

profile in the Benjamin's sense. Hence, describing the interface flow in the transformed co-ordinate system is the appropriate approach.

Let us now give attention to the mean velocity profile parameter C. The value of C found in table 1 is 8·62. Stewart (1970) found $C = 7{\cdot}2$ for smooth flat water surface and $C = 3{\cdot}7$ for mechanically generated water waves. He stated that the lower value

of $C = 3{\cdot}7$ resulted from the roughness created by the mechanically generated water waves and concluded that 'the velocity profile over water waves is quantitatively similar to the profile over a rough plate'. We disagree! From the wave-following property of the mean profiles, the surface roughness should be that produced by the ripples riding on the generated water wave. The ripple roughness in this study and also in Stewart's corresponded to an aerodynamically smooth surface. If the generated water waves are regarded as surface roughness, we also expect that the C value should continuously decrease as the wind speed is increased when the wave amplitude is kept constant because the relative roughness given by $a^+ = au_*/\nu$ is larger at higher wind speed. This was not observed by Stewart.

The lower value of $C = 3{\cdot}7$ in Stewart's results was a consequence of his fixed-probe measurements. The mean velocity measured in the fixed frame is smaller than that measured in the transformed frame and the difference of the two-frame measurements increases as one approaches the interface. This gives a considerably lower C for the fixed-frame result.

On the other hand, our 8·62 and Stewart's 7·2 for C are considerably higher than that generally accepted for flow over a smooth solid wall. This may be due to the existence of the drift current at the interface. The drift current releases a portion of the turbulent shear stress to give a lower value of u_* for interface flows than that for smooth, solid wall (flat or wavy) flows. Accordingly, curve-fitting by profile method results in a lower slope u_*/k_0 and a higher intercept C. Taking the surface drift current into account, we find

$$C = C^{\circ} + \frac{U_0}{u_*} + \Delta C, \tag{5.1}$$

where C° is the C value for flow over smooth wall and ΔC is the change in C due to the shear stress relaxation (see Hsu *et al.* 1977). Assuming $U_0/U_\infty = 0{\cdot}03$, we find $C = 6{\cdot}91$ if $C^{\circ} = 5{\cdot}0$ (Hussain & Reynolds 1970) and $C = 8{\cdot}11$ if $C^{\circ} = 6{\cdot}2$ (Coles 1954). Considering the scatter in C°, our result for C and Stewart's 7.2 are not inconsistent with the stress relief hypothesis.

5.2. *Comparison of wave perturbation field to fixed-frame results*

As stated in § 2, measurements of $\tilde{u}_i(x, y, t)$ in the fixed frame should be comparable to $\tilde{u}_i^*(x^*, y^*, t^*)$ if condition (2.16) is satisfied, i.e. if the wave amplitude is much less than the viscous sublayer thickness. The amplitudes and the phases of $\tilde{u}^*$ and $\tilde{v}^*$ based on (2.15*a*, *b*) were calculated and are shown in figures 13(*a*, *b*). The results are compared to the fixed probe measurements of Stewart (1970) for his case of $U_\infty = 120$ cm s^{-1} ($U_\infty/c = 1{\cdot}51$, $ka = 0{\cdot}10$ and $y_c^+ = y_c u_*/\nu \simeq 40$, where $U(y_c) = c$). No agreement is found and the discrepancy may arise because condition (2·16) is not satisfied.

The model predictions by Davis (1970), which Stewart compared to his data, are also shown in figures 13(*a*, *b*) (only Stewart's case for $\delta = 15{\cdot}0$ and $\gamma = 3{\cdot}51$). Two models were calculated by Davis: model *A* is the quasi-laminar model with

$$\tilde{r}_{ij}(x, y, t) = 0$$

and model *B* is the closure model proposed by Davis (1970) using Benjamin's wave-following profile concepts (quasi-laminar model in the transformed co-ordinate system). While Stewart found his data compared better to the prediction of model *B*,

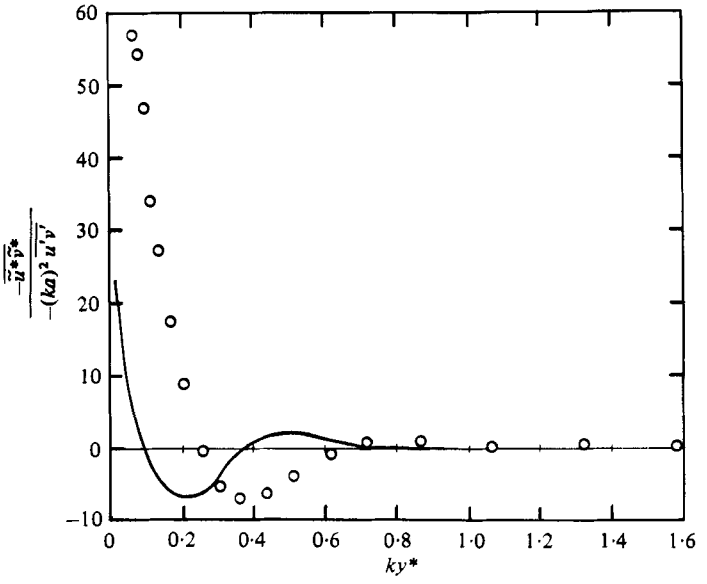

FIGURE 14. Distribution of the wave-associated Reynolds stress $-\overline{\tilde{u}^*\tilde{v}^*}$ and its comparison to the prediction by Townsend (1972). ○, this experiment, $C/u_* = 18{\cdot}2$; ——, Townsend, $C/u_* = 16$.

we find model A, a model in which the induced-turbulent-Reynolds stresses are not zero in the transformed co-ordinate system, is in better agreement with our data. However, the agreement is only qualitative. The inconsistency in this comparison also raises the following question: Which set of data, $\tilde{u}_i(x,y,t)$ or $\tilde{u}_i^*(x^*,y^*,t^*)$, is more proper for comparison to the results of a fixed frame closure model? Although we have shown that $\tilde{u}_i^*$ may be more suitable, further measurements both in (x,y,t) and (x^*,y^*,t^*) and more comparisons to realistic closure models are required.

The transformed wave-associated Reynolds stress $-\overline{\tilde{u}^*\tilde{v}^*}$ normalized by $-\overline{u'v'}(ka)^2$ is plotted in figure 14. The predicted result by Townsend (1972) for $c/u_* = 16$ is also included. They agree in the trend of the variation but not in the magnitude. Near the interface, the measured values are considerably higher than the predicted ones. However, it can be argued that the kinetic energy closure model of Townsend has to some degree described correctly the wave perturbed interface flow fields. The improvement on this model by Gent & Taylor (1976) gives better predictions on wave growth rate and supports this argument.

5.3. *Momentum transfer*

The momentum transfer across the interface is produced by viscous, pressure and turbulent forces acting at the interface. If one neglects the viscous stress outside the viscous sublayer, the total momentum transfer is given by

$$(-\rho\overline{u'v'} + \overline{\tilde{p}\,\partial\tilde{\eta}/\partial x} + \rho\overline{\tilde{r}_{11}\,\partial\tilde{\eta}/\partial x})_{y^*=\delta_0},$$

where $-\rho\overline{u'v'}|_{y^*=\delta_0}$ is the momentum supported by the surface drift current and

$$(\overline{\tilde{p}\,\partial\tilde{\eta}/\partial x} + \rho\overline{\tilde{r}_{11}\,\partial\tilde{\eta}/\partial x})_{y^*=\delta_0} = \rho(-\overline{\tilde{u}\tilde{v}} + \overline{\tilde{\eta}\,\partial\tilde{r}_{12}/\partial y^*})_{y^*=\delta_0} \tag{5.2}$$

is the momentum supported by the waves. Our results for $\tilde{r}_{ij}$ show that the turbulent transfers are one order smaller than $-\rho\tilde{\tilde{u}}\tilde{\tilde{v}}|_{y^*=\delta_0}$; hence, to the first order, (5.2) reduces to the inviscid quasi-laminar expression,

$$\overline{\tilde{p}\,\partial\tilde{\eta}/\partial x}|_{y^*=\delta_0} = -\rho\tilde{\tilde{u}}\tilde{\tilde{v}}|_{y^*=\delta_0}, \tag{5.3}$$

and the total momentum transfer is given by $-\rho(\overline{u'v'}+\tilde{\tilde{u}}\tilde{\tilde{v}})_{y^*=\delta_0}$.

In § 4·3(*b*), we showed that $-\overline{u'v'}|_{y^*=\delta_0}/U_\infty^2 = 1{\cdot}3\times10^{-3}$. The value of $-\tilde{\tilde{u}}\tilde{\tilde{v}}|_{y^*=\delta_0}/U_\infty^2$ obtained by extrapolating the profiles of $-\tilde{\tilde{u}}\tilde{\tilde{v}}$ given in figure 5.11 of Hsu *et al.* (1977) is $9{\cdot}6\times10^{-4}$; it is probable that the extrapolation produces an error of less than 10 % because the data for $-\tilde{\tilde{u}}\tilde{\tilde{v}}$ form a fairly smooth curve†. Thus, the ratio of momentum flux to the wave field to the total momentum flux across the interface, as given by

$$\gamma_M = \frac{\tilde{\tilde{u}}\tilde{\tilde{v}}|_{y^*=\delta_0}}{(\overline{u'v'}+\tilde{\tilde{u}}\tilde{\tilde{v}})_{y^*=\delta_0}} \tag{5.4}$$

is found to be 0·42 for this experiment.

5.4. *The structure of the critical layer*

In the quasi-laminar theory, the critical layer is produced by viscous effects which smooth the discontinuity at $y = y_c$ which arises from the inviscid assumption. How the energy and momentum are exchanged by fluid elements when they pass across the viscous critical layer was well interpreted by Lighthill (1962). The mean streamlines observed in a frame moving with wave celerity exhibit the so-called 'cat's-eye' pattern near the critical height. The cat's-eye of Lighthill is located right above the wave crest and the closed loop circulation in the cat's-eye is symmetrical. However, Stewart (1974) pointed out that, if diffusion of vorticity is assumed, the closed loop circulation must be asymmetrical. Since the mean velocity profile follows the wave form, the critical layer is located at $y^* = y_c^*$, where $U(y_c^*) = c$. A sketch of the mean streamline pattern for an undulating asymmetrical critical layer can be found in figure 6(*c*) of Stewart (1974).

Norris & Reynolds (1975) predicted the cat's-eye patterns in a transformed coordinate system. The distinct feature of their predictions is that the cat's-eye is forced by the mean flow downwind from the wave crest, viz. on the lee-ward side for a quasi-laminar model and at the wave trough for both turbulent kinetic energy and eddy viscosity models. However, their cat's-eye patterns are confined in a thin layer in the proximity of the interface. The possibility that the cat's-eye may be located in the trough was first suggested by Stewart (1967) from the flow separation over a cavity in a wall. A cat's-eye pattern over breaking waves was also proposed by Banner & Melville (1976) based on their visual study. The cat's-eye patterns for breaking waves correspond to air flow separation; there are stagnation points at the interface and the 'cat's-eyes' are directly attached to the interface. A discussion on separated and unseparated flows and their associated cat's-eye patterns was also given by Gent & Taylor (1977).

From our measured values of U, $\tilde{u}$ and $\tilde{v}$, we are able to construct a cat's-eye pattern for our flow. The result is shown in figure 15 where the dotted line indicates the

† The profile of $-\tilde{\tilde{u}}\tilde{\tilde{v}}$ shown here in figure 7 represents only one of the four profiles given in Hsu *et al.* (1977).

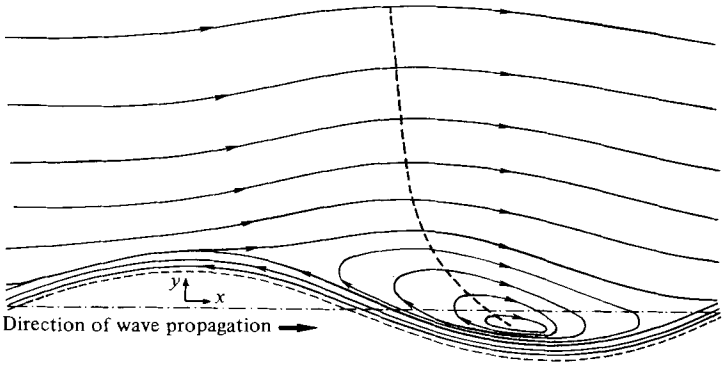

FIGURE 15. Sketch of streamline pattern as observed in the frame moving with the wave speed.

locations of $\tilde{v} = 0$ such that the tangent to the streamlines is horizontal. The locations where the closed loop circulations reverse the flow direction were determined from $U + \tilde{u} - c = 0$. As shown in figure 15, the 'cat's-eye' is located in the wave trough and is considerably thicker than the predictions by Norris & Reynolds (1975). Our cat's-eye pattern resembles that predicted by Gent & Taylor (1977).

The thicker critical layer may be the consequence of turbulent mixing which takes over the role of the viscous diffusion in smoothing the discontinuity resulting from the inviscid analysis. The critical height of the viscous critical layer is shifted up and down according to $U + \tilde{u} + u' - c = 0$. The range of the instantaneous critical height shifts is usually larger than the thickness of the viscous critical layer. Furthermore, as a result of mixing the structure of the local viscous critical layer may be strongly changed due to the vertical transport by $\tilde{v} + v'$. The statistically averaged result is then a turbulently mixed critical layer. Although the critical height may still occur most probably at y_c^*, the effective mean critical height $\bar{y}_c^*$ of the turbulently mixed critical layer is different from y_c^* because the probabilistic distribution of the instantaneous critical height is expected to be asymmetrical in the vertical direction. $\bar{y}_c^*$ is higher than y_c^* if y_c^* is located at the lower edge of the turbulent boundary layer and vice versa. The mean velocity profile shown in figure 3 gives $y_c^+ = 46{\cdot}7$ when

$$u^+ = c^+ = 18{\cdot}2.$$

From the prediction of Davis' model A, the viscous critical layer ranges approximately from $y^+ = 30$–60. On the other hand, the continuous phase shift in $\theta_{\tilde{u}^*}$ and $\theta_{\tilde{v}^*}$ indicates the turbulently mixed critical layer ranges from $y^+ = 30$ to 700. Because the quasi-laminar model (model A) predicted a minimum value for $|\hat{v}^*|$ at y_c^+, it is plausible to assume that the effective critical height is located where the measured $|\hat{v}^*|$ for turbulent boundary layer flow is a minimum. From figure 13, the effective critical height is located approximately at $\bar{y}_c^+ = 350$. The critical layer is broadened by turbulent mixing as pointed out by Lighthill (1962). As a result, the Reynolds stress $-\overline{\tilde{u}^*\tilde{v}^*}$ varies continuously over the entire boundary layer, and one does not observe the sharp change at y_c^* predicted by inviscid analysis.

It is also expected that the closed loop circulation will be deeper for higher wave amplitude because $\tilde{u}$ is as effective as u' in shifting the critical height. This effect of

wave amplitude on the cat's-eye pattern was studied by Gent & Taylor (1977). Their numerical model produced a thicker critical layer for larger wave amplitude.

6. Conclusions

A set of experiments were run in a large laboratory facility with a turbulent wind blowing over a 1 Hz, small-amplitude, mechanically generated water wave. Our analysis of the data in the context of several theoretical constructs suggests the following:

(1) The mean velocity profile is basically log-linear. The turbulent shear stress $-\rho\overline{u'v'}$ is partially released by the existence of the drift current at the interface and by the wave-propagation behaviour. As a result, the value of u_* is lower than and the value of C is higher than those measured for turbulent flows over a flat plate.

(2) The mean flow near the interface appears to follow the wave form but that in the free stream does not; hence, describing the interface flow in the transformed co-ordinate system is clearly an appropriate approach.

(3) At the wind speed of this study (2·4 m s^{-1}) the roughness produced by ripples is not large enough to interfere with the wind field. Close examination of the mean flow indicates that the mechanically generated water wave should not be considered as portion of the surface roughness. Thus, the surface condition is aerodynamically smooth.

(4) In this experiment, the wave-induced motion in the air near the free stream is irrotational. In the boundary layer, the motion is rotational with strong production of the wave-associated Reynolds stress $-\rho\tilde{u}\tilde{v}$. Most of $-\rho\tilde{u}\tilde{v}$ is produced in the proximity of the interface. A phase jump of 180° was observed for the induced turbulent Reynolds stresses $\tilde{r}_{ij}$ at $ky^* = 0{\cdot}6$.

(5) The wave-induced turbulent Reynolds stresses $\tilde{r}_{ij}$ make a negligible contribution ($< 10\,\%$ of the wave-associated Reynolds stress) to the momentum transfer at the interface. Thus, the ratio of momentum flux to the wave field to the total momentum flux across the interface is given by the ratio of $\overline{\tilde{u}\tilde{v}}|_{y^*=\delta_0}$ to $(\overline{u'v'}+\overline{\tilde{u}\tilde{v}})_{y^*=\delta_0}$ and is about 0·42.

This work was supported by the National Science Foundation through Grant NSF-ENG-76-15106, the Office of Naval Research through Contract N00014-76-C-0155, and the U.S. Army Research Office through Grant DAAG29-76-G-0125.

REFERENCES

Acharya, M. & Reynolds, W. C. 1975 Measurements and predictions of a fully developed turbulent channel flow with imposed controlled oscillations. *Stanford Univ., Dept Mech. Engng, Tech. Rep.* no. TF-8.

Banner, M. L. & Melville, W. K. 1976 On the separation of air flow over water waves. *J. Fluid Mech.* **77**, 825–842.

Barnett, T. P. & Wilkerson, J. C. 1967 On the generation of ocean wind waves as inferred from airborne radar measurements of fetch-limited spectra. *J. Mar. Res.* **25**, 292–321.

Bendat, J. S. & Piersol, A. G. 1971 *Random Data: Analysis and Measurement Procedures.* Wiley-Interscience.

Benjamin, T. B. 1959 Shearing flow over a wavy boundary. *J. Fluid Mech.* **6**, 161–205.

BOLE, J. B. & HSU, E. Y. 1969 Response of gravity water waves to wind excitation. *J. Fluid Mech.* **35**, 657–675.

COLES, D. E. 1954 The problem of the turbulent boundary layer. *Z. angew. Math. Phys.* **5**, 181–203.

COLES, D. W. 1956 The law of the wake in the turbulent boundary layer. *J. Fluid Mech.* **1**, 191–226.

COLONELL, J. M. 1966 Laboratory simulation of sea waves. *Stanford Univ., Dept Civil Engng, Tech. Rep.* no. 65.

DAVIS, R. E. 1970 On the turbulent flow over a wavy boundary. *J. Fluid Mech.* **42**, 721–731.

DAVIS, R. E. 1972 On prediction of the turbulent flow over a wavy boundary. *J. Fluid Mech.* **52**, 287–306.

DOBSON, F. W. 1971 Measurements of atmospheric pressure on wind-generated sea waves. *J. Fluid Mech.* **48**, 91–127.

DOBSON, F. W. & ELLIOTT, J. A. 1978 Wave-pressure correlation measurements over growing sea waves with a wave follower and fixed height pressure sensors. In *Turbulent Fluxes Through the Sea Surface, Wave Dynamics and Prediction* (ed. A. Favre & K. Hasselmann), pp. 421–432. Plenum.

ELLIOTT, J. 1972 Microscale pressure fluctuations near waves being generated by the wind. *J. Fluid Mech.* **54**, 427–448.

GENT, P. R. 1977 A numerical model of the air flow above water waves. Part 2. *J. Fluid Mech.* **82**, 349–369.

GENT, P. R. & TAYLOR, P. A. 1976 A numerical model of the air flow above water waves. *J. Fluid Mech.* **77**, 105–128.

GENT, P. R. & TAYLOR, P. A. 1977 A note on 'separation' over short wind waves. *Boundary-Layer Met.* **11**, 65–87.

HASSELMANN, K., BARNETT, T. P., BOUWS, E., CARLSON, H., CARTWRIGHT, D. E., ENKE, K., EWING, J. A., GIENAPP, H., HASSELMANN, D. E., KRUSEMAN, P., MEERBURG, A., MÜLLER, P., OLBERS, D. J., RICHTER, K., SELL, W., & WALDEN, H. 1973 Measurements of wind-wave growth and swell decay during the Joint North Sea Wave Project. *Deutsches Hydrographisches Institut.* Hamburg.

HINZE, J. O. 1975 *Turbulence – An Introduction to Its Mechanism and Theory.* McGraw-Hill.

HSU, E. Y. 1965 A wind, water-wave research facility. *Stanford Univ., Dept Civil Engng, Tech. Rep.* no. 57.

HSU, C. T., HSU, E. Y. & STREET, R. L. 1977 The structure of modulated turbulent flow over progressive water waves. *Stanford Univ., Dept Civil Engng, Tech. Rep.* no. 221.

HUSSAIN, A. K. M. F. & REYNOLDS, W. C. 1970 The mechanics of an organized wave in turbulent shear flow. *J. Fluid Mech.* **41**, 241–258.

KENDALL, J. M. 1970 The turbulent boundary layer over a wall with progressive surface waves. *J. Fluid Mech.* **41**, 259–281.

KLEBANOFF, P. S. 1955 Characteristics of turbulence in a boundary layer with zero pressure gradient. *N.A.C.A. Rep.* no. 1247.

LIGHTHILL, M. J. 1962 Physical interpretation of the mathematical theory of wave generation by wind. *J. Fluid Mech.* **14**, 385–398.

LIU, J. T. C. & MERKINE, L. 1976 On the interactions between large-scale structure and fine-grained turbulence in a free shear flow. I. The development of temporal interactions in the mean. *Proc. Roy. Soc.* A **352**, 213–247.

LONG, R. B. 1971 On generation of ocean waves by a turbulent wind. Ph.D. dissertation, University of Miami.

LONGUET-HIGGINS, M. S. 1969 Action of a variable stress at the surface of water waves. *Phys. Fluids* **12**, 737–740.

MILES, J. W. 1957 On the generation of surface waves by shear flows. *J. Fluid Mech.* **3**, 185.

MILES, J. W. 1959 On the generation of surface waves by shear flows. Part 2. *J. Fluid Mech.* **6**, 568–582.

MILES, J. W. 1967 On the generation of surface waves by shear flows. Part 5. *J. Fluid Mech.* **30**, 163–175.

NORRIS, H. L. & REYNOLDS, W. C. 1975 Turbulent channel flow with a moving wavy boundary. *Stanford Univ., Dept Mech. Engng, Tech. Rep.* no. TF-7.

PHILLIPS, O. M. 1957 On the generation of surface waves by turbulent wind. *J. Fluid Mech.* **2**, 417–445.

PHILLIPS, O. M. 1977 *The Dynamics of the Upper Ocean*, 2nd ed. Cambridge University Press.

SAEGER, J. C. & REYNOLDS, W. C. 1971 Perturbation pressures over traveling sinusoidal waves with fully developed turbulent shear flow. *Stanford Univ., Dept Mech. Engng, Rep.* no. FM-9.

SCHLICHTING, H. 1968 *Boundary Layer Theory*. McGraw-Hill.

SNYDER, R. L. 1974 A field study of wave-induced pressure fluctuations above surface gravity waves. *J. Mar. Res.* **32**, 497–531.

SNYDER, R. L. & COX, C. S. 1966 A field study of the wind generation of ocean waves. *J. Mar. Res.* **24**, 141–178.

STEWART, R. H. 1970 Laboratory studies of the velocity field over deep-water waves. *J. Fluid Mech.* **42**, 733–754.

STEWART, R. W. 1967 Mechanics of air-sea interface. *Phys. Fluids Suppl.* **10**, S47–55.

STEWART, R. W. 1974 The air–sea momentum exchange. *Boundary-Layer Met.* **6**, 151–167.

TAKEUCHI, K. & MOGEL, T. R. 1975 A performance evaluation of a mini-computer. *Rev. Sci. Instrum.* **46**, 686–691.

TOWNSEND, A. A. 1972 Flow in a deep turbulent boundary layer over a surface distorted by water waves. *J. Fluid Mech.* **55**, 719–753.

WU, J. 1968 Laboratory studies of wind–wave interactions. *J. Fluid Mech.* **34**, 91–111.

YU, H. Y., HSU, E. Y. & STREET, R. L. 1971 A refined measurement of aerodynamic pressure over progressive water waves. *Stanford Univ., Dept Civil Engng, Rep.* no. 146.